

# RG-Invariant Symmetry Ratio for QCD: A Study of $U(1)_A$ and Chiral Symmetry Restoration

Ting-Wai Chiu,<sup>a,b,c,d,e,1</sup> Tung-Han Hsieh<sup>f</sup>

<sup>a</sup>*Nuclear Science Division, Lawrence Berkeley National Laboratory, Berkeley, CA 94720*

<sup>b</sup>*Department of Physics, National Taiwan University, Taipei, Taiwan 10617*

<sup>c</sup>*Institute of Physics, Academia Sinica, Taipei, Taiwan 11529*

<sup>d</sup>*Department of Physics, National Taiwan Normal University, Taipei, Taiwan 11677*

<sup>e</sup>*Physics Division, National Center for Theoretical Sciences, Taipei, Taiwan 10617*

<sup>f</sup>*Research Center for Applied Sciences, Academia Sinica, Taipei, Taiwan 11529*

*E-mail:* [twchiu@phys.ntu.edu.tw](mailto:twchiu@phys.ntu.edu.tw), [thhsieh@gate.sinica.edu.tw](mailto:thhsieh@gate.sinica.edu.tw)

**ABSTRACT:** We introduce a renormalization-group invariant observable, the symmetry strength parameter  $\kappa_{AB}$ , for the quantitative characterization of symmetry breaking in QCD. As a first application, we employ  $\kappa_{AB}$  to investigate the relative strength of  $SU(2)_L \times SU(2)_R$  chiral symmetry and  $U(1)_A$  axial symmetry breaking in  $N_f = 2 + 1 + 1$  lattice QCD using optimal domain-wall fermions at the physical point. Our study covers three lattice spacings and twelve temperatures in the range 164–385 MeV. We examine three independent symmetry-breaking channels in the nonsinglet sector with quark-connected correlators: the  $U(1)_A$ -sensitive scalar–pseudoscalar channel ( $\kappa_{PS}$ ), probing the  $\pi$ – $\delta$  system; the  $SU(2)_L \times SU(2)_R$ -sensitive vector–axial-vector channel ( $\kappa_{VA}$ ), probing the  $\rho$ – $a_1$  system; and an additional  $U(1)_A$ -sensitive tensor–axial-tensor channel ( $\kappa_{TX}$ ), probing the  $\rho_T$ – $b_1$  system. At finite lattice spacing, we observe a clear hierarchy  $\kappa_{PS} > \kappa_{VA} > \kappa_{TX}$ . A controlled continuum extrapolation reveals that this hierarchy collapses, with all three symmetry-breaking strengths becoming statistically indistinguishable within our precision. This result provides a new, model-independent benchmark from a chirally symmetric lattice action. Our findings indicate that the effective restoration scales for  $SU(2)_L \times SU(2)_R$  and  $U(1)_A$  in the nonsinglet sector converge closely near the chiral crossover, placing stringent quantitative constraints on the temperature window for chiral and axial symmetry breaking in quark-connected channels. These results support a two-stage restoration scenario, in which full symmetry restoration—including the singlet sector—occurs only at significantly higher temperatures once topological fluctuations are sufficiently suppressed.

---

<sup>1</sup>Corresponding author.

---

## Contents

<b>1</b>	<b>Introduction</b>	<b>1</b>
<b>2</b>	<b>RG-invariant symmetry ratio</b>	<b>3</b>
2.1	Correlation functions and symmetry partners	3
2.2	Renormalization and RG invariance	4
2.3	Integrated spectral weights and the symmetry strength parameter	6
2.4	Susceptibility symmetry relations	8
<b>3</b>	<b>Lattice setup</b>	<b>10</b>
<b>4</b>	<b>Results</b>	<b>12</b>
<b>5</b>	<b>Continuum limit</b>	<b>15</b>
<b>6</b>	<b>Discussion and Outlook</b>	<b>18</b>
6.1	Connections to topological susceptibility and singlet sector	19
6.2	Hierarchical restoration of chiral and axial symmetries	20
6.3	Broader symmetry landscape and emergent phases above $T_c$	22
6.4	Future computational improvements and extensions	23
6.5	RG interpretation and comparison with Pisarski–Wilczek analyses	24
6.6	Concluding remarks	26
<b>A</b>	<b>Meson Operator Notation</b>	<b>28</b>
<b>B</b>	<b>Tables of results</b>	<b>29</b>

---

## 1 Introduction

The pattern of symmetry realization is a defining feature of any quantum field theory, governing its phase structure and the spectrum of its excitations. In Quantum Chromodynamics (QCD), the theory of the strong interaction, two global symmetries play a pivotal role: the chiral  $SU(2)_L \times SU(2)_R$  symmetry of the light ( $u, d$ ) quark sector, and the  $U(1)_A$  axial symmetry. In the vacuum, the former is spontaneously broken by the chiral condensate  $\langle \bar{q}q \rangle$  [1, 2], giving mass to nucleons and generating pions as pseudo-Goldstone bosons. The latter is explicitly broken by the axial anomaly [3–5], contributing significantly to the mass of the  $\eta'$  meson [6–8]. A cornerstone of modern nuclear physics is understanding how these broken symmetries behave under extreme conditions of temperature and density, such as those realized in heavy-ion collisions or within neutron stars.

The restoration of chiral symmetry is associated with the transition from a hadronic phase to a quark-gluon plasma (QGP). For QCD with physical quark masses, this is a smooth crossover occurring at a temperature  $T_c \sim 156$  MeV [9–13].

A profound and long-standing question is whether the effective restoration of the  $U(1)_A$  symmetry, linked to the suppression of topological gauge fluctuations, coincides with this chiral crossover or occurs at a distinctly higher temperature  $T_1 > T_c$  [14–17]. Resolving this hierarchy is essential for a complete understanding of the QGP’s structure, the nature of the QCD transition, and the validity of effective models. Progress on this question via first-principles lattice QCD simulations has been challenging. A consistent picture among them has not emerged yet, see e.g., refs. [18–26], and the recent review [27].

The  $U(1)_A$  anomaly is particularly sensitive to lattice artifacts, and its clean study requires fermion discretizations that preserve chiral symmetry. Lattice studies with chiral fermions (domain-wall [28, 29] or overlap [30, 31]) have provided crucial insights [18, 19, 21, 24–26]. Notably, the JLQCD collaboration, using  $N_f = 2$  Möbius domain-wall fermions with reweighting for overlap fermions at the lattice spacing 0.07 fm, found clear evidence that for  $T > 190$  MeV, the  $U(1)_A$  breaking is consistent with zero within statistical errors [24]. This is also consistent with studies using  $N_f = 2 + 1 + 1$  optimal domain-wall fermions at the physical point and lattice spacing 0.064 fm, where  $U(1)_A$  axial symmetry is restored for  $T \gtrsim 190$  MeV [25]. However, refs. [24, 25] have not determined the  $U(1)_A$  symmetry breaking for  $T < 190$  MeV. On the other hand, in ref. [26], using  $N_f = 2 + 1$  Möbius domain-wall fermions at multiple lattice spacings, the authors observed that the  $U(1)_A$  axial symmetry is not restored for  $T \lesssim 186$  MeV. To investigate whether any discrepancies between these different studies would occur for  $T < 190$  MeV, a systematic approach to obtain definite continuum-extrapolated results for physical QCD with a chirally symmetric action remains a high-priority goal for the community. Addressing this goal requires overcoming two interconnected challenges: first, performing controlled continuum extrapolations across the temperature range of interest; second, developing a robust, quantitative observable to compare symmetry-breaking strength across different channels.

Traditional probes, such as hadron thermal and screening masses or the behavior of specific correlation functions at a fixed Euclidean distance, can be ambiguous or sensitive to analysis choices. What is needed is a *renormalization-group (RG) invariant* measure that integrates spectral information, provides a clear normalization, and allows for a direct comparison between  $SU(2)_L \times SU(2)_R$  and  $U(1)_A$  breaking.

In this paper, we address both challenges. First, we introduce a novel, universal diagnostic: the *RG-invariant symmetry ratio*  $\kappa_{AB}$ . For two operators  $A$  and  $B$  related by a symmetry transformation, we define  $\kappa_{AB} = (\chi_A - \chi_B)/(\chi_A + \chi_B)$ , where  $\chi_A \geq \chi_B > 0$  denote the corresponding regularized susceptibilities. This construct is bounded  $\kappa_{AB} \in [0, 1]$ , and crucially RG-invariant for exact symmetry partners, making it an ideal model-independent probe.

Second, we present the first application of  $\kappa_{AB}$  to the problem of symmetry restoration in QCD. We perform lattice simulations with  $N_f = 2 + 1 + 1$  optimal domain-wall quarks at the physical point, using three lattice spacings and twelve temperatures in the range 164–385 MeV. We compute  $\kappa_{AB}$  across three distinct symmetry-breaking channels in the

*nonsinglet* sector: the  $U(1)_A$ -breaking (scalar, pseudoscalar) channel ( $\kappa_{PS}$ ) probing the  $\pi$ - $\delta$  system; the  $SU(2)_L \times SU(2)_R$ -breaking (vector, axial-vector) channel ( $\kappa_{VA}$ ) probing the  $\rho$ - $a_1$  system; and an additional  $U(1)_A$ -sensitive channel using tensor–axial-tensor operators ( $\kappa_{TX}$ ) which probes the  $\rho$ - $b_1$  system through the  $\bar{q}\gamma_4\gamma_k q$  and  $\bar{q}\gamma_5\gamma_4\gamma_k q$  currents. The inclusion of the tensor channel provides a vital cross-check, as it probes the  $U(1)_A$  anomaly through a different Dirac structure than the scalar channel.

Our key findings are as follows. At finite lattice spacing, we observe a clear ordering:  $\kappa_{PS} > \kappa_{VA} > \kappa_{TX}$ , where the breaking in the  $U(1)_A$  scalar–pseudoscalar channel is strongest, while the  $U(1)_A$  tensor–axial-tensor channel is significantly weaker than the other two channels. However, a controlled continuum extrapolation reveals that this entire hierarchy collapses. All three symmetry-breaking strengths become statistically indistinguishable within our resolution. This result provides a new, high-precision benchmark from a chirally symmetric action. It indicates that the effective restoration scales probed by these different operators converge in the continuum limit, suggesting that the manifestations of  $SU(2)_L \times SU(2)_R$  and  $U(1)_A$  symmetries in the *nonsinglet* sector are much more concurrent than suggested by finite-lattice-spacing studies focused on a single channel.

The paper is organized as follows. In section 2, we formally define the RG-invariant symmetry ratio  $\kappa_{AB}$  and detail its theoretical properties. Our lattice setup, time-correlation functions, and analysis methodology are described in section 3. Numerical results at finite lattice spacing are presented in section 4, and the continuum extrapolation is performed in section 5. The implications of our findings and future applications of the  $\kappa_{AB}$  framework are discussed in section 6.

## 2 RG-invariant symmetry ratio

We introduce a renormalization-group invariant quantity that quantifies the degree of symmetry breaking in a quantum field theory. The construction relies on integrated spectral weights of Euclidean correlation functions for symmetry-related operators. Our measure, the *symmetry strength parameter*  $\kappa_{AB}$ , provides a global, scale-free indicator of symmetry violation and will be applied later to chiral symmetry restoration in finite-temperature QCD.

### 2.1 Correlation functions and symmetry partners

In a theory with an exact symmetry, correlation functions of operators related by the symmetry transformation must be degenerate. Consider the Euclidean time correlation function of a local meson operator

$$O_{\Gamma}^a(\vec{x}, t) = \bar{q}(\vec{x}, t) \Gamma t^a q(\vec{x}, t),$$

where  $\Gamma$  is a Dirac matrix specifying the quantum numbers of the channel,  $t^a$  (with  $a = 1, \dots, N_f^2 - 1$ ) are the generators of  $SU(N_f)$  for flavor nonsinglets, and  $t^0 \equiv \text{diag}(1, 1, \dots, 1) / \sqrt{2N_f}$  (identity operator) for the flavor singlet, with the normalization condition  $\text{tr}(t^a t^b) = \delta^{ab} / 2$  ( $a = 0, \dots, N_f^2 - 1$ ). For flavor-singlet operators we adopt the shorthand notation  $\bar{q}\Gamma q \equiv \bar{q}\Gamma t^0 q$ , with the factor  $t^0$  always implied but suppressed. For flavor nonsinglet operators,

there are  $N_f(N_f - 1)$  off-diagonal ones with off-diagonal  $t^a$  (e.g.,  $t_1 = \tau_1/2$  and  $t_2 = \tau_2/2$  in  $SU(2)$ ) and  $(N_f - 1)$  diagonal ones with diagonal  $t^a$  (e.g.,  $t_3 = \tau_3/2$  in  $SU(2)$ ).

We use the notation  $(x_1, x_2, x_3, x_4) \equiv (x, y, z, t) \equiv (\vec{x}, t)$  interchangeably. With this notation, the  $t$ -correlator is defined as

$$C_\Gamma(t) = \int d^3x [\langle O_\Gamma^a(\vec{x}, t) O_\Gamma^a(\mathbf{0}, 0) \rangle - \langle O_\Gamma^a \rangle^2], \quad (2.1)$$

and its spatial counterpart, the  $z$ -correlator, as

$$C_\Gamma(z) = \int dx dy dt [\langle O_\Gamma^a(x, y, z, t) O_\Gamma^a(\mathbf{0}, 0) \rangle - \langle O_\Gamma^a \rangle^2]. \quad (2.2)$$

Here  $\langle O_\Gamma^a \rangle \equiv v_A$  is the vacuum expectation value (VEV) of the operator, and the subtraction  $-v_A^2$  removes the factorized (constant) piece from the correlator. Note that for flavor-singlet and diagonal nonsinglet operators, the full expectation value  $\langle O(\vec{x}, t) O(0) \rangle$  receives contributions from both quark-connected and quark-disconnected Wick contractions. The terminology “quark-disconnected” refers solely to the quark-line topology; on each gauge configuration  $U$ , the quark propagator  $D^{-1}(U; x, y)$  is fully dressed by gluon interactions, and the gauge average  $\langle \dots \rangle_U$  includes the fermion determinant  $\det[D(U)]$  which generates all virtual quark-loop effects. For most channels  $v_A = 0$  by symmetry (except scalar singlet with any quark masses, and scalar diagonal nonsinglets with nondegenerate quark masses), eqs. (2.1)–(2.2) reduce to  $\langle OO \rangle$ . If a symmetry is exact, the correlators of two partners  $A$  and  $B$  satisfy  $C_A(t) = C_B(t)$  for any  $t$  and  $C_A(z) = C_B(z)$  for any  $z$ .

Composite operators such as  $O_\Gamma^a(x)$  require regularization and renormalization. Both  $C_\Gamma(t)$  and  $C_\Gamma(z)$  contain short-distance singularities; the leading divergence behaves as  $t^{-3}$  or  $z^{-3}$  in the continuum limit as the two operators approach coincidence. In what follows we concentrate on the  $t$ -correlator; the extension to the  $z$ -correlator is straightforward.

## 2.2 Renormalization and RG invariance

To quantify the deviation from degeneracy at a specific Euclidean time one may define a pointwise ratio

$$\kappa_{AB}(t) = \frac{C_A(t) - C_B(t)}{C_A(t) + C_B(t)}, \quad t \neq 0. \quad (2.3)$$

An analogous ratio  $\kappa_{AB}(z)$  for spatial correlators has been employed to study  $U(1)_A$  and  $SU(2)_L \times SU(2)_R$  symmetry patterns in thermal QCD with optimal domain-wall fermions [32, 33].

At fixed  $t \neq 0$ , the two operators in  $C_\Gamma(t)$  are separated by a nonzero Euclidean distance, so the correlator is free of additive UV divergences — no subtraction is required. The only UV issue is the multiplicative renormalization factor  $Z_A^2$  from the anomalous dimension of the composite operator. This factor cancels in the ratio  $\kappa_{AB}(t)$  when  $Z_A = Z_B$ , making  $\kappa_{AB}(t)$  RG-invariant without any reference-temperature subtraction. Additive divergences arise only upon integration over  $t$  (the accumulation of the  $C(t) \sim 1/t^3$  singularity as  $t \rightarrow 0$  generates a  $\sim 1/a^2$  divergence in the integrated susceptibility), and their removal is the subject of section 2.3.

**Equality of renormalization constants from symmetry.** If two operators  $O_A$  and  $O_B$  are related by a symmetry transformation that is respected by the regularized action, their renormalization constants are equal:  $Z_A = Z_B$ . This is a purely UV property — it depends only on the short-distance structure of the regularized theory, not on the state of the system. In particular:

- *Spontaneous symmetry breaking does not affect  $Z_A = Z_B$ .* SSB is an infrared property of the vacuum state; the UV counterterms are determined by the action alone.
- *The  $U(1)_A$  anomaly does not affect  $Z_A = Z_B$ .* The anomaly is a finite, one-loop exact effect that modifies Ward identities at finite distances but does not alter the UV divergent structure.
- *Non-degenerate quark masses do not affect  $Z_A = Z_B$  in any mass-independent renormalization scheme (e.g., RI-MOM [34])*

The crucial requirement is that the *regularization* preserves the symmetry. For overlap or domain-wall fermions, the Ginsparg-Wilson relation ensures that chiral symmetry is an exact symmetry of the lattice action, so  $Z_A = Z_B$  holds for all chiral partners in any mass-independent scheme.

Furthermore, since the quark-gluon vertex is flavor-blind, the anomalous dimension  $\gamma_O$  of the composite operator  $\bar{q}\Gamma t^a q$  depends only on the Dirac structure  $\Gamma$ , not on the flavor matrix  $t^a$ . Consequently, the renormalization constant is the same for singlet ( $t^0$ ) and nonsinglet ( $t^a$ ,  $a \geq 1$ ) operators with the same  $\Gamma$ :

$$Z_\Gamma^s = Z_\Gamma^{ns} \quad (\text{any } N_f, \text{ any quark masses}).$$

Combining this with the chiral partner relations  $Z_S = Z_P$  and  $Z_T = Z_X$  from the Ginsparg-Wilson symmetry gives:

$$Z_S^{ns} = Z_P^{ns} = Z_S^s = Z_P^s, \quad Z_T^{ns} = Z_X^{ns} = Z_T^s = Z_X^s, \quad (2.4)$$

which hold for *any*  $N_f$  and any quark masses in a mass-independent scheme with chirally symmetric regularization.

For vector and axial-vector channels, the flavor-blind relation  $Z_\Gamma^s = Z_\Gamma^{ns}$  combines with Ward identities and the Ginsparg-Wilson symmetry to give a particularly simple result. The nonsinglet vector current  $\bar{q}\gamma_\mu t^a q$  is the Noether current of  $SU(2)_V$ , which is exactly conserved for all  $m_q$  (with degenerate quarks), giving  $Z_V^{ns} = 1$ . The nonsinglet axial-vector current  $\bar{q}\gamma_5\gamma_\mu t^a q$  is the Noether current of  $SU(2)_A$ ; it is conserved only in the chiral limit ( $\partial^\mu A_\mu^a = 2m_q\bar{q}\gamma_5 t^a q$ ), but has no anomaly (since  $\text{tr}(t^a) = 0$ ). In a mass-independent scheme,  $Z$  does not depend on  $m_q$ , so  $Z_A^{ns} = 1$  for all  $m_q$ . Equivalently, the Ginsparg-Wilson relation gives  $Z_A^{ns} = Z_V^{ns} = 1$  directly. The singlet vector current  $\bar{q}\gamma_\mu q$  is conserved by the exact  $U(1)_V$  symmetry, giving  $Z_V^s = 1$ . For the singlet axial-vector current  $h_{1\mu} \sim \bar{q}\gamma_5\gamma_\mu q$ , the  $U(1)_A$  anomaly makes the current non-conserved:  $\partial^\mu h_{1\mu} = 2\bar{q}\gamma_5 M q + N_f \frac{g^2}{16\pi^2} F\tilde{F}$ , where  $M$  is the diagonal mass matrix. However, the anomaly is a finite, one-loop exact effect that

does not introduce new UV divergences. The flavor-blind argument therefore still applies, giving  $Z_A^s = Z_A^{ns} = 1$ . In summary, for chirally symmetric regularizations:

$$Z_V^{ns} = Z_V^s = Z_A^{ns} = Z_A^s = 1. \quad (2.5)$$

(Note: in continuum schemes where  $\gamma_5$  is ill-defined in  $d \neq 4$  dimensions, such as the Larin prescription in  $\overline{\text{MS}}$  [35], a scheme-dependent renormalization  $Z_A^s \neq 1$  can appear. This subtlety is absent for Ginsparg-Wilson fermions, where  $\gamma_5$  is well-defined on the lattice.) Note that both the singlet vector current  $\bar{q}\gamma_\mu q$  and the singlet axial-vector current  $\bar{q}\gamma_5\gamma_\mu q$  are invariant under  $U(1)_A$  (since  $\{\gamma_5, \gamma_\mu\} = 0$ ), so they are *not*  $U(1)_A$  partners and the ratio  $\kappa_{\omega, h_1}$  does *not* probe  $U(1)_A$  restoration.

These relations ensure that the ratio  $\kappa_{AB}(t)$  in eq. (2.3) is RG-invariant for any pair of operators from the same renormalization constant multiplet, as the common factor  $Z_A^2 = Z_B^2$  cancels between numerator and denominator.

**Correlator symmetry relations.** When a symmetry is effectively restored at temperature  $T$ , the correlators of symmetry partners become degenerate:  $C_A(t, T) = C_B(t, T)$  for all  $t$ . The specific partner identifications depend on the number of flavors through the generators  $t^a$  of the flavor group  $SU(N_f)$ .

In what follows we specialize to  $N_f = 2$ , where the nonsinglet generators are  $t^a = \tau^a/2$  ( $a = 1, 2, 3$ , with  $\tau^a$  the Pauli matrices) and  $t^0 = \mathbf{1}/2$  for the singlet. Effective restoration of  $SU(2)_L \times SU(2)_R$  implies

$$C_S^s(t) = C_P^{ns}(t) \iff C_\sigma(t) = C_\pi(t), \quad (2.6)$$

$$C_P^s(t) = C_S^{ns}(t) \iff C_\eta(t) = C_\delta(t), \quad (2.7)$$

$$C_{T_k}^s(t) = C_{X_k}^{ns}(t) \iff C_{\omega_T}(t) = C_{b_1}(t), \quad k = 1, 2, 3, \quad (2.8)$$

$$C_{X_k}^s(t) = C_{T_k}^{ns}(t) \iff C_{h_{1T}}(t) = C_{\rho_T}(t), \quad k = 1, 2, 3, \quad (2.9)$$

$$C_{V_k}^{ns}(t) = C_{A_k}^{ns}(t) \iff C_\rho(t) = C_{a_1}(t), \quad k = 1, 2, 3, \quad (2.10)$$

and effective restoration of  $U(1)_A$  implies

$$C_S^{ms}(t) = C_P^{ms}(t) \iff C_\delta(t) = C_\pi(t), \quad (2.11)$$

$$C_S^s(t) = C_P^s(t) \iff C_\sigma(t) = C_\eta(t), \quad (2.12)$$

$$C_{T_k}^{ms}(t) = C_{X_k}^{ms}(t) \iff C_{\rho_T}(t) = C_{b_1}(t), \quad k = 1, 2, 3, \quad (2.13)$$

$$C_{T_k}^s(t) = C_{X_k}^s(t) \iff C_{\omega_T}(t) = C_{h_{1T}}(t), \quad k = 1, 2, 3, \quad (2.14)$$

where the superscripts  $s$  and  $ns$  denote singlet and nonsinglet channels, respectively. Each pair of (2.6)-(2.14) corresponds to a distinct ratio  $\kappa_{AB}(t)$  as defined in eq. (2.3). The notations of meson operators are summarized in appendix A.

### 2.3 Integrated spectral weights and the symmetry strength parameter

Although  $\kappa_{AB}(t)$  is a valid probe, its dependence on  $t$  and the statistical fluctuations at individual times make a channel-wide comparison of symmetry breaking cumbersome. A more robust global measure is obtained by integrating over Euclidean time, which sums

the spectral weight in each channel. We therefore define the *bare susceptibility* for channel  $A$  at temperature  $T$  with the  $t = 0$  contact term excluded (the  $n = 0$  time slice includes the coincident-point singularity, contributing  $a \cdot C(0) \sim 1/a^2$  to  $\chi$  even in the free theory; excluding it removes this divergence):

$$\chi_A(T) = \int_{0 < t < 1/T} dt C_A(t, T), \quad (2.15)$$

where  $C_A(t, T)$  is the correlator (2.1) at temperature  $T$ . Since the VEV subtraction  $-\langle O \rangle_T^2$  is already built into the definition of  $C_A(t, T)$ , no additional vacuum subtraction is needed here. For channels where  $v_A = 0$  (all off-diagonal nonsinglet channels, and most singlet and diagonal nonsinglet channels), the VEV term is absent and  $C_A(t, T)$  reduces to  $\int d^3x \langle OO \rangle$ . For channels where  $v_A \neq 0$  (the scalar singlet  $\sigma$  for any quark masses, and scalar diagonal nonsinglets for non-degenerate quark masses), the VEV must be measured on the lattice and subtracted as part of the correlator construction.

The *regularized susceptibility* is defined as the difference with respect to a reference temperature  $T_r \gg T_c$  at which the symmetry is effectively restored:

$$\chi_A^{\text{reg}}(T; T_r) \equiv \chi_A(T) - \chi_A(T_r). \quad (2.16)$$

All UV divergences in  $\chi_A(T)$  are independent of temperature [36–40], and therefore the additive divergences cancel in  $\chi_A^{\text{reg}}$ , rendering it multiplicative renormalizable.

The reference temperature  $T_r$  should be chosen sufficiently above  $T_c$  such that the symmetry is effectively restored. The continuum extrapolation is insensitive to the precise choice of  $T_r$  as long as it lies in the symmetry restored phase. In this study, we take  $aT_r = 1/4$ , where  $\chi_A = \chi_B$  within uncertainties, for all  $SU(2)_L \times SU(2)_R$  and  $U(1)_A$  nonsinglet channels  $PS$ ,  $VA$  and  $TX$ .

Note that in thermal QCD, one commonly removes the additive UV divergences by subtracting the zero-temperature value,  $\chi^{\text{reg0}}(T) \equiv \chi(T) - \chi(0)$ , since all UV divergences are temperature-independent. The regularization defined in eq. (2.16) is then the difference of the commonly regularized observables,  $\chi^{\text{reg}}(T; T_r) = \chi^{\text{reg0}}(T) - \chi^{\text{reg0}}(T_r)$ , which is the most natural choice for the RG-invariant measure  $\kappa_{AB}$ .

**Multiplicative renormalization.** The renormalized operator is  $O_A^R = Z_A(\mu_R, a) O_A^{\text{bare}}$  where  $\mu_R$  is the renormalization scale, and  $Z_A$  is the renormalization constant which in general is logarithmic divergent except for the conserved vector and axial-vector currents with  $Z_A = 1$ . Correspondingly, the renormalized susceptibility is

$$\chi_A^R(T; T_r; \mu_R) = Z_A^2(\mu_R, a) \chi_A^{\text{reg}}(T; T_r). \quad (2.17)$$

For the ratio  $\kappa_{AB}$  with  $Z_A = Z_B$  (as guaranteed for symmetry partners; see section 2.2), the common factor  $Z_A^2$  cancels and no determination of  $Z_A$  is needed. An analogous definition holds for channel  $B$ .

Because  $Z_A = Z_B$  for symmetry partners and  $\chi_A^{\text{reg}}$  is multiplicatively renormalizable, we can now construct a global, RG-invariant measure of symmetry breaking, the *symmetry*

strength parameter:

$$\kappa_{AB}(T) = \frac{\chi_A^{\text{reg}}(T; T_r) - \chi_B^{\text{reg}}(T; T_r)}{\chi_A^{\text{reg}}(T; T_r) + \chi_B^{\text{reg}}(T; T_r)}, \quad (2.18)$$

where  $\chi_A^{\text{reg}} \geq \chi_B^{\text{reg}} \geq 0$  (by convention) and  $0 \leq \kappa_{AB} \leq 1$ .

**RG invariance.** Since  $Z_A = Z_B$  for symmetry partners, the common factor  $Z_A^2$  cancels between numerator and denominator of  $\kappa_{AB}$ :

$$\kappa_{AB}(T) = \frac{\chi_A^R(T) - \chi_B^R(T)}{\chi_A^R(T) + \chi_B^R(T)}, \quad (2.19)$$

where  $\chi_A^R = Z_A^2 \chi_A^{\text{reg}}$  as defined in eq. (2.17). No non-perturbative renormalization (NPR) is needed to evaluate  $\kappa_{AB}$ . The parameter  $\kappa_{AB}$  provides an intuitive scale:  $\kappa_{AB} = 0$  indicates exact degeneracy of the regularized susceptibilities (the symmetry is manifest), whereas  $\kappa_{AB} \rightarrow 1$  signals maximal asymmetry.

The construction of  $\kappa_{AB}$  is general and can be applied to study any symmetry in quantum field theory for which symmetry partner operators can be defined.

**Remark on terminology.** Throughout this work, “restoration” of a symmetry always refers to *effective restoration* — i.e., the corresponding RG-invariant ratio  $\kappa_{AB}$  becomes consistent with zero within statistical uncertainties. Exact restoration, which would require vanishing quark masses for  $SU(2)_L \times SU(2)_R$  and additionally the complete suppression of the  $U(1)_A$  anomaly for  $U(1)_A$  restoration, is neither achievable in physical QCD nor required for the validity of our conclusions. This operational definition is implicit in all subsequent uses of “degeneracy”, “restoration”, and “ $\kappa_{AB} = 0$ ”. Note that  $\kappa_{AB} = 0$  means the regularized susceptibilities  $\chi_A^{\text{reg}}$  and  $\chi_B^{\text{reg}}$  are equal at temperature  $T$ , i.e., channel  $A$  and channel  $B$  carry the same integrated spectral weight above the restored baseline  $T_r$ .

In the remainder of this paper we employ  $\kappa_{AB}$  to investigate the restoration patterns of the  $U(1)_A$  and  $SU(2)_L \times SU(2)_R$  symmetries in high-temperature lattice QCD.

**Notation.** From this point on, all susceptibilities are understood to be regularized (i.e.,  $\chi_A \equiv \chi_A^{\text{reg}}(T; T_r)$  as defined in eq. (2.16)), with the superscript “reg” and the arguments  $(T; T_r)$  suppressed for brevity.

## 2.4 Susceptibility symmetry relations

The full chiral  $SU(2)_L \times SU(2)_R$  multiplet for  $J = 0$  mesons includes not only the quark-connected channels studied in this work, but also symmetry pairs involving flavor-singlet operators (see eqs. (2.6)-(2.10)). In principle, each pair could be probed by the symmetry ratio  $\kappa_{AB}$  defined in eq. (2.18), offering additional insight into chiral restoration. Integrating the correlator symmetry relations of section 2.2 over Euclidean time yields the corresponding susceptibility equalities.

For  $N_f = 2$  QCD, effective restoration of  $SU(2)_L \times SU(2)_R$  chiral symmetry (eqs. (2.6)–

(2.10)) implies:

$$\chi_S^s = \chi_P^{ns} \iff \chi_\sigma = \chi_\pi, \quad (2.20)$$

$$\chi_P^s = \chi_S^{ns} \iff \chi_\eta = \chi_\delta, \quad (2.21)$$

$$\chi_{T_k}^s = \chi_{X_k}^{ns} \iff \chi_{\omega_T} = \chi_{b_1}, \quad k = 1, 2, 3, \quad (2.22)$$

$$\chi_{X_k}^s = \chi_{T_k}^{ns} \iff \chi_{h_{1T}} = \chi_{\rho_T}, \quad k = 1, 2, 3, \quad (2.23)$$

$$\chi_{V_k}^{ns} = \chi_{A_k}^{ns} \iff \chi_\rho = \chi_{a_1}, \quad k = 1, 2, 3, \quad (2.24)$$

where the superscripts  $s$  and  $ns$  denote singlet and nonsinglet channels, respectively. Recall that the physical  $\eta'$  corresponds to the  $\eta$  singlet in  $N_f = 2$  QCD. The notations of meson operators and their corresponding regularized susceptibilities are summarized in appendix A.

On the other hand, effective restoration of  $U(1)_A$  axial symmetry (eqs. (2.11)–(2.14)) implies:

$$\chi_S^{ns} = \chi_P^{ns} \iff \chi_\delta = \chi_\pi, \quad (2.25)$$

$$\chi_S^s = \chi_P^s \iff \chi_\sigma = \chi_\eta, \quad (2.26)$$

$$\chi_{T_k}^{ns} = \chi_{X_k}^{ns} \iff \chi_{\rho_T} = \chi_{b_1}, \quad k = 1, 2, 3, \quad (2.27)$$

$$\chi_{T_k}^s = \chi_{X_k}^s \iff \chi_{\omega_T} = \chi_{h_{1T}}, \quad k = 1, 2, 3. \quad (2.28)$$

Each equality of (2.20)–(2.28) corresponds to a distinct RG-invariant symmetry ratio  $\kappa_{AB}$  as defined in eq. (2.18). Since  $Z_A = Z_B$  for all these symmetry pairs (established in section 2.2), *any* ratio  $\kappa_{AB}$  involving operators from the same renormalization constant multiplet is RG-invariant. This includes the nonsinglet ratios  $\kappa_{PS}$ ,  $\kappa_{VA}$ ,  $\kappa_{TX}$  studied in this work, as well as singlet-involved ratios such as  $\kappa_{\sigma,\pi}$ ,  $\kappa_{\eta,\delta}$ ,  $\kappa_{\omega_T,b_1}$ ,  $\kappa_{h_{1T},\rho_T}$ ,  $\kappa_{\sigma,\eta}$  and  $\kappa_{\omega_T,h_{1T}}$ . Consequently, ratios like  $\kappa_{\sigma,\pi}$  and  $\kappa_{\eta,\delta}$  are formally RG-invariant, just like their nonsinglet counterparts.

Despite this formal RG invariance, practical extraction of  $\kappa_{AB}$  for channels involving flavor-singlet operators is challenging in current lattice simulations. Singlet correlators receive contributions from quark-disconnected Wick contractions, which are computationally demanding and statistically noisy. For the scalar singlet  $\sigma \sim \bar{q}q$ , the nonvanishing VEV  $v_\sigma = \langle \bar{q}q \rangle_T$  must additionally be measured and subtracted at both  $T$  and  $T_r$ . These computational difficulties are the main obstacles; the renormalization of singlet channels is no more complicated than that of nonsinglet channels, since  $Z_A = Z_B$  for all symmetry pairs (section 2.2).

Given these considerations, the present study focuses initially on the quark-connected, nonsinglet channels where the RG-invariant ratio  $\kappa_{AB}$  rests on the firmest theoretical and numerical ground:

- $\kappa_{PS}$  ( $\delta$ - $\pi$ ) for  $U(1)_A$ ,
- $\kappa_{VA}$  ( $\rho$ - $a_1$ ) for  $SU(2)_L \times SU(2)_R$ ,
- $\kappa_{TX}$  ( $\rho_T$ - $b_1$ ) for  $U(1)_A$  through a different Dirac structure.

These choices provide a clean, theoretically unambiguous, and statistically precise set of observables. The consistent picture emerging from these three channels (presented in section 4 and section 5) gives strong evidence for the relative restoration scales of  $U(1)_A$  and  $SU(2)_L \times SU(2)_R$  symmetries.

### 3 Lattice setup

We generate gauge ensembles using hybrid Monte Carlo (HMC) simulations of lattice QCD with  $N_f = 2 + 1 + 1$  optimal domain-wall quarks [41, 42] at the physical point. The simulations are performed on  $32^3 \times (16, 12, 10, 8, 4)$  lattices with the plaquette gauge action [43] at three values of  $\beta = 6/g^2 = (6.15, 6.18, 6.20)$ , corresponding to lattice spacings  $a \simeq (0.075, 0.069, 0.064)$  fm. These ensembles are produced with the same actions [44, 45] and algorithms as their counterparts on larger  $64^3 \times (20, 16, 12, 10, 8, 6)$  lattices [46], but at one-eighth of the spatial volume. Simulations are carried out on GPU clusters equipped with various NVIDIA GPUs.

After initial thermalization, gauge configurations are sampled and distributed among 16–32 independent simulation units, each performing a separate HMC stream. In each stream, one configuration is sampled every five trajectories. All sampled configurations from all streams are combined to obtain the final ensemble. Lattice parameters and statistics for the meson  $t$ -correlator calculations are listed in table 1. The temperatures covered range from  $\sim 164$  to 385 MeV, all above the pseudocritical temperature  $T_c \sim 150$  MeV.

Lattice spacings and quark masses ( $u/d$ ,  $s$ ,  $c$ ) are determined on  $32^3 \times 64$  lattices with  $\{460, 636, 726\}$  configurations for  $\beta = \{6.15, 6.18, 6.20\}$ , respectively. The lattice spacing

$\beta$	$a[\text{fm}]$	$N_x$	$N_t$	$T[\text{MeV}]$	$N_{\text{confs}}$	$(m_{u/d}a)_{\text{res}}$	$(m_s a)_{\text{res}}$	$(m_c a)_{\text{res}}$
6.15	0.075	32	16	164	359	$6.2(5) \times 10^{-5}$	$3.1(4) \times 10^{-5}$	$1.1(7) \times 10^{-5}$
6.18	0.069	32	16	179	324	$4.9(7) \times 10^{-5}$	$5.8(1.7) \times 10^{-5}$	$2.7(9) \times 10^{-5}$
6.20	0.064	32	16	192	588	$3.5(4) \times 10^{-5}$	$2.3(2) \times 10^{-5}$	$6.5(1.1) \times 10^{-6}$
6.15	0.075	32	12	219	409	$9.0(1.4) \times 10^{-5}$	$6.0(8) \times 10^{-5}$	$1.5(3) \times 10^{-6}$
6.18	0.069	32	12	238	781	$1.9(2) \times 10^{-5}$	$1.6(1) \times 10^{-5}$	$3.8(5) \times 10^{-6}$
6.20	0.064	32	12	257	514	$1.8(6) \times 10^{-5}$	$1.6(6) \times 10^{-5}$	$9.4(4.2) \times 10^{-6}$
6.15	0.075	32	10	263	496	$2.4(4) \times 10^{-5}$	$2.0(3) \times 10^{-5}$	$7.5(2.6) \times 10^{-6}$
6.18	0.069	32	10	286	377	$2.4(8) \times 10^{-5}$	$2.2(7) \times 10^{-5}$	$9.7(3.9) \times 10^{-6}$
6.20	0.064	32	10	308	481	$5.8(1.5) \times 10^{-6}$	$5.1(1.2) \times 10^{-6}$	$1.4(2) \times 10^{-6}$
6.15	0.075	32	8	328	640	$3.5(8) \times 10^{-5}$	$2.9(6) \times 10^{-5}$	$1.2(3) \times 10^{-5}$
6.18	0.069	32	8	357	302	$1.3(7) \times 10^{-5}$	$1.2(6) \times 10^{-5}$	$4.9(2.2) \times 10^{-6}$
6.20	0.064	32	8	385	468	$6.3(1.9) \times 10^{-6}$	$6.0(1.8) \times 10^{-6}$	$3.0(9) \times 10^{-6}$
6.15	0.075	32	4	657	413	$4.5(1) \times 10^{-5}$	$4.5(1) \times 10^{-5}$	$9.4(3) \times 10^{-7}$
6.18	0.069	32	4	715	763	$1.0(1) \times 10^{-6}$	$1.0(1) \times 10^{-6}$	$1.0(1) \times 10^{-6}$
6.20	0.064	32	4	770	991	$1.2(2) \times 10^{-6}$	$1.2(2) \times 10^{-6}$	$1.2(2) \times 10^{-6}$

**Table 1:** Lattice parameters and statistics of the fifteen gauge ensembles used in this work. The last three columns give the residual masses of  $u/d$ ,  $s$ , and  $c$  quarks [50].

$\beta$	$a[\text{fm}]$	$m_{u/d}a$	$m_s a$	$m_c a$
6.15	0.0751(5)	0.00200	0.064	0.705
6.18	0.0690(5)	0.00180	0.058	0.626
6.20	0.0641(4)	0.00125	0.040	0.550

**Table 2:** Lattice spacings and bare quark masses for  $N_f = 2 + 1 + 1$  lattice QCD with optimal domain-wall quarks at the physical point.

is fixed using the Wilson flow [47, 48] with the condition  $\{t^2\langle E(t)\rangle\}|_{t=t_0} = 0.3$  and input  $\sqrt{t_0} = 0.1416(8)$  fm [49]. The resulting spacings are listed in table 2. Physical quark masses are obtained by tuning the bare masses so that the lowest-lying states extracted from time-correlation functions of the meson operators  $\{\bar{u}\gamma_5 d, \bar{s}\gamma_i s, \bar{c}\gamma_i c\}$  agree with the physical masses of  $\pi^\pm(140)$ ,  $\phi(1020)$ , and  $J/\psi(3097)$ . The tuned bare quark masses are also given in table 2.

Chiral symmetry breaking due to the finite extent  $N_s = 16$  in the fifth dimension is quantified by the residual masses of each quark flavor [50], listed in the last three columns of table 1. These residual masses are less than (4.5%, 0.1%, 0.005%) of the corresponding bare masses for ( $u/d, s, c$ ) quarks, translating to less than (0.2, 0.1, 0.06) MeV/ $c^2$ , respectively. This confirms that chiral symmetry is well preserved and that the effective 4D Dirac operator for optimal domain-wall fermions remains accurate for both light and heavy quarks. Consequently, hadronic observables (such as meson correlators) can be computed with high precision, with uncertainties dominated by statistics and other systematics.

We now summarize the notations and conventions used in this work.

The correlation function of off-diagonal flavor-nonsinglet meson interpolator  $\bar{q}_1\Gamma q_2$  (e.g.,  $\bar{u}\Gamma d$ ) on a lattice with  $(N_x, N_y, N_z, N_t)$  sites is computed as

$$C_\Gamma(x) = \langle (\bar{q}_1\Gamma q_2)_x (\bar{q}_1\Gamma q_2)_0^\dagger \rangle = \left\langle \text{tr} \left[ \Gamma (D_c + m_1)_{0,x}^{-1} \Gamma (D_c + m_2)_{x,0}^{-1} \right] \right\rangle_{\text{confs}}, \quad (3.1)$$

where  $(D_c + m_q)^{-1}$  denotes the valence quark propagator with mass  $m_q$  in lattice QCD with exact chiral symmetry [51],  $\text{tr}$  is the trace over color and Dirac indices, and  $\langle \dots \rangle_{\text{confs}}$  denotes the average over gauge configurations. Here  $x = (x_1, x_2, x_3, x_4) = (x, y, z, t)$ ; an overall sign arising from  $\gamma_4\Gamma^\dagger\gamma_4 = \pm\Gamma$  has been suppressed. The temporal correlator is defined as

$$C_\Gamma(t, T) = \sum_{x_1, x_2, x_3} C_\Gamma(x), \quad (3.2)$$

where  $T = 1/(N_t a)$  is the temperature. The bare susceptibility (2.15) can be written as

$$\chi_\Gamma(T) = \sum_{t=1}^{N_t-1} C_\Gamma(t, T). \quad (3.3)$$

In this study we focus on the off-diagonal flavor-nonsinglet operator  $\bar{u}\Gamma d/\sqrt{2}$ , with

$$\Gamma = \{\mathbf{1}, \gamma_5, \gamma_k, \gamma_5\gamma_k, \gamma_4\gamma_k, \gamma_5\gamma_4\gamma_k, k = 1, 2, 3\},$$

corresponding to the scalar (S), pseudoscalar (P), vector (V), axial-vector (A), tensor-vector (T), and axial-tensor-vector (X) channels, respectively.

Thanks to  $S_3$  symmetry, the correlators satisfy  $C_{V_1} = C_{V_2} = C_{V_3}$ ,  $C_{A_1} = C_{A_2} = C_{A_3}$ ,  $C_{T_1} = C_{T_2} = C_{T_3}$ , and  $C_{X_1} = C_{X_2} = C_{X_3}$ . To improve statistics, we average over the three spatial components for each channel, e.g.,

$$C_V(t, T) = \frac{1}{3} \sum_{k=1}^3 C_{V_k}(t, T),$$

and similarly for  $A$ ,  $T$  and  $X$ .

These averaged correlators  $C_\Gamma(t, T)$  are used to compute the regularized susceptibility of off-diagonal flavor nonsinglet mesons,

$$\chi_\Gamma(T) = \sum_{t=1}^{N_t-1} [C_\Gamma(t, T) - C_\Gamma(t, T_r)], \quad (3.4)$$

where  $aT_r = 1/4$  is the reference temperature at which chiral symmetries are highly restored. The RG-invariant symmetry ratios  $\kappa_{AB}$  defined in eq. (2.18) are then computed for the channel pairs  $VA$ ,  $PS$ , and  $TX$ . Here  $\kappa_{VA}$  probes  $SU(2)_L \times SU(2)_R$  chiral symmetry restoration, while  $\kappa_{PS}$  and  $\kappa_{TX}$  probe  $U(1)_A$  axial symmetry restoration.

## 4 Results

We begin by analyzing the temporal correlators  $C_\Gamma(t)$  of the  $\bar{u}\Gamma d$  bilinears at the three lowest temperatures,  $T = (164, 179, 192)$  MeV, displayed in figure 1. Our focus is on the degeneracy patterns among the  $(V, A)$ ,  $(P, S)$ , and  $(T, X)$  channels, which reflect the restoration of  $SU(2)_L \times SU(2)_R$  chiral symmetry (probed by  $V$ - $A$  degeneracy) and  $U(1)_A$  axial symmetry (probed by  $P$ - $S$  and  $T$ - $X$  degeneracy).

As shown in figure 1, the correlators follow the ordering

$$C_P(t) \gtrsim C_S(t) > C_V(t) \gtrsim C_A(t) > C_T(t) \gtrsim C_X(t)$$

at all temperatures. This hierarchy corresponds to the ordering of meson thermal masses,

$$m_P \lesssim m_S < m_V \lesssim m_A < m_T \lesssim m_X,$$

which remains consistent across the full temperature range studied (164–385 MeV).

Within the resolution of our data, no splitting is observed inside the  $(P, S)$ ,  $(V, A)$ , or  $(T, X)$  doublets, except for a mild deviation in the  $(P, S)$  channel at  $T = 164$  MeV on the coarsest lattice ( $a = 0.075$  fm), shown in the upper panel of figure 1. Since degeneracy in the  $(P, S)$  and  $(T, X)$  channels signals  $U(1)_A$  restoration, the observed discrepancy is likely a lattice artifact due to finite lattice spacing.

To cleanly address this issue in the continuum limit, a renormalization-group (RG) invariant measure of degeneracy is required—one that can be extrapolated to  $a \rightarrow 0$  and allows quantitative comparison of symmetry breaking across different channels. Standard

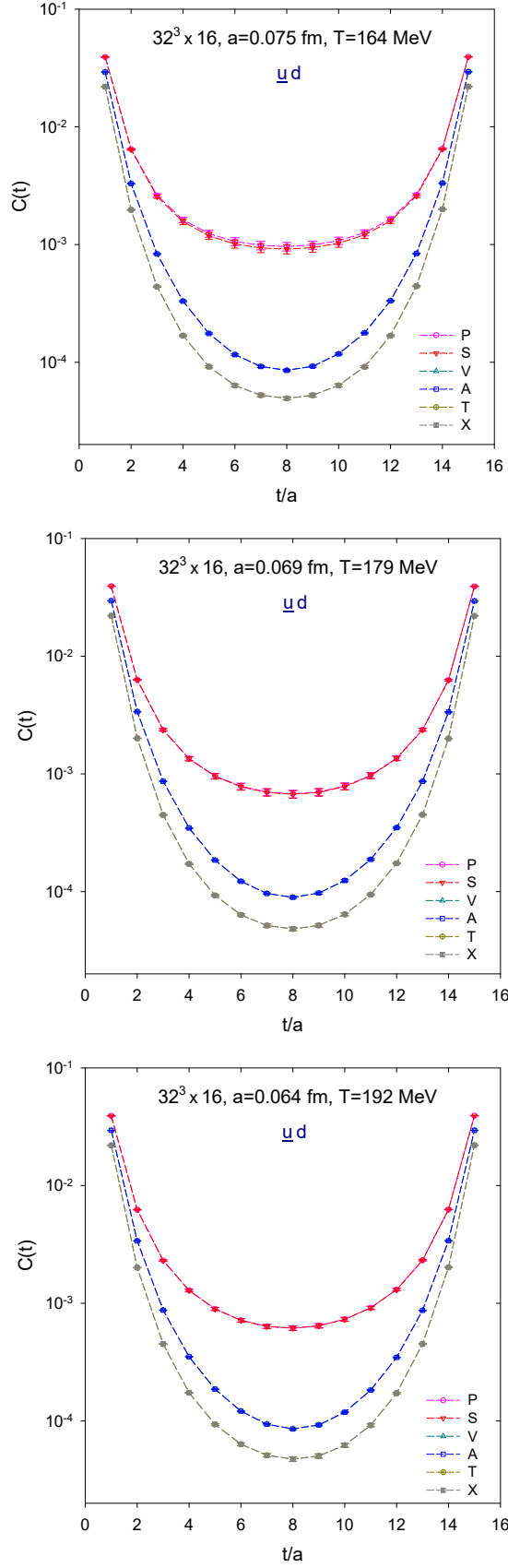


**Figure 1:**  $t$ -correlators of  $\bar{u}\Gamma d$  at the three lowest temperatures. The dashed lines connecting the data points in each channel are shown only to guide the eye.

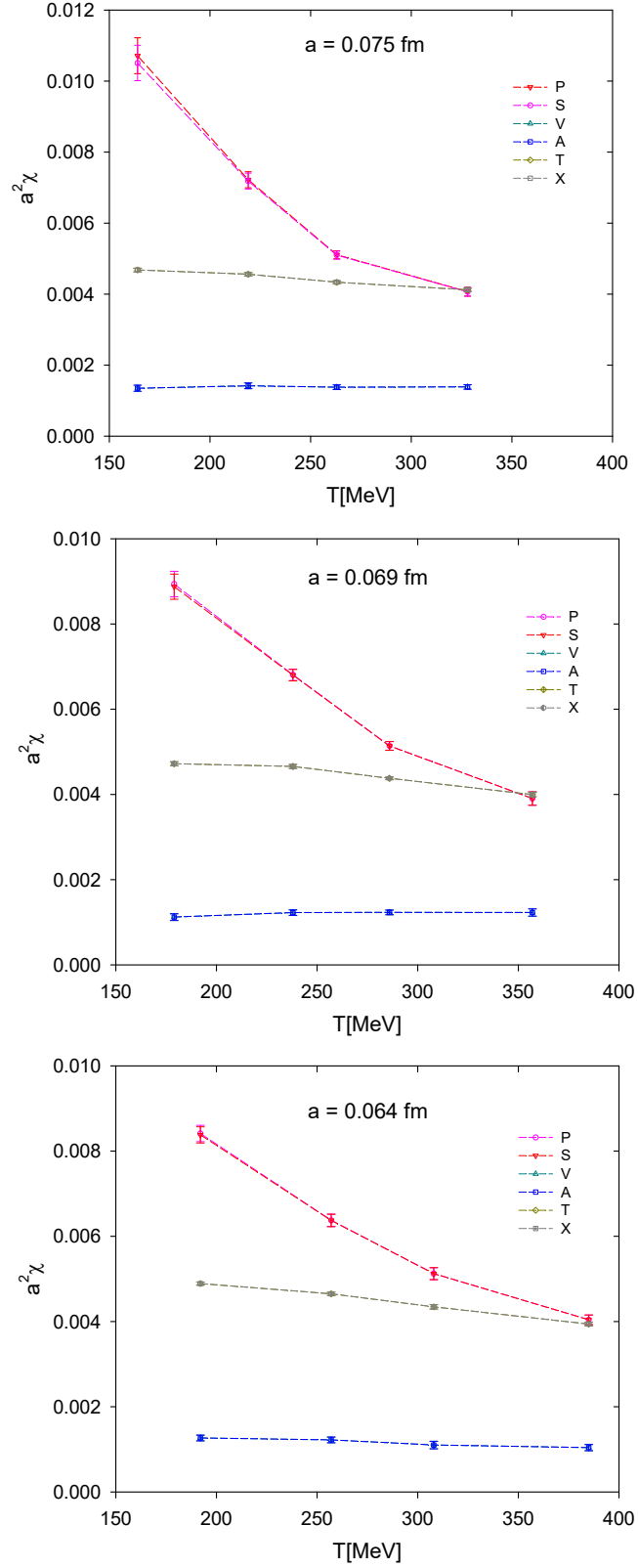


**Figure 2:** Regularized susceptibilities of  $\bar{u}\Gamma d$  (3.4) for three lattice spacings  $a=(0.075, 0.069, 0.064)$  fm and twelve temperatures from 164–385 MeV. The dashed lines connecting the data points in each channel are shown only to guide the eye.

probes, such as thermal hadron masses or single-time correlator values, can be ambiguous or sensitive to analysis details. Instead, we employ the RG-invariant symmetry ratio  $\kappa_{AB}$  defined in eq. (2.18), which integrates spectral information, provides clear normalization, and enables direct comparison between  $SU(2)_L \times SU(2)_R$  and  $U(1)_A$  breaking in all channels.

Accordingly, we compute the regularized susceptibilities (3.4)  $\chi_P, \chi_S, \chi_V, \chi_A, \chi_T$ , and  $\chi_X$ , shown in figure 2, as well as the RG-invariant symmetry ratios  $\kappa_{PS}, \kappa_{VA}$ , and  $\kappa_{TX}$  presented in figure 3. These quantities are obtained for three lattice spacings  $a = (0.075, 0.069, 0.064)$  fm and twelve temperatures from 164 to 385 MeV.

Numerical values of the correlators, bare susceptibilities (3.3) at the reference temperature  $aT_r = 1/4$ , regularized susceptibilities (3.4), and symmetry ratios are provided in appendix B.

In figure 2, the regularized susceptibilities show no splitting within any doublet, again except for the  $(P, S)$  channel at  $T = 164$  MeV on the coarsest lattice. This aligns with the behavior seen in the correlators and reinforces the interpretation that the observed  $(P, S)$  deviations at the lowest temperature are artifacts of finite lattice spacing.

From figure 3, a clear hierarchy emerges:

$$\kappa_{PS} > \kappa_{VA} > \kappa_{TX},$$

which holds for all three lattice spacings and across the entire temperature range. If one were to use  $\kappa_{PS}$  and  $\kappa_{VA}$  at finite  $a$  as measures of  $U(1)_A$  and  $SU(2)_L \times SU(2)_R$  breaking, respectively, the data would suggest that  $U(1)_A$  restoration occurs at a higher temperature than chiral symmetry restoration. On the other hand, using  $\kappa_{TX}$  as the  $U(1)_A$  indicator would imply that  $SU(2)_L \times SU(2)_R$  is restored at a higher temperature than the  $U(1)_A$  restoration. This apparent contradiction can only be resolved by taking the continuum limit, which we address in the next section.

## 5 Continuum limit

After testing the data for  $\kappa_{PS}(a, T)$ ,  $\kappa_{VA}(a, T)$ , and  $\kappa_{TX}(a, T)$  against various models, we find that at fixed lattice spacing  $a$ , the temperature dependence of each  $\kappa$  can be well described by a simple power law:

$$\kappa(a, T) = A(a)(T[\text{GeV}])^{-B(a)}, \quad (5.1)$$

where the temperature  $T$  is expressed in GeV.

For each lattice spacing, we first extract the parameters  $A(a)$  and  $B(a)$  via a log—log fit:

$$\ln \kappa(a, T) = \ln A(a) - B(a) \ln (T[\text{GeV}]).$$

The resulting fitted parameters  $A(a)$  and  $B(a)$ , together with the corresponding  $\chi^2/\text{dof}$ , are summarized for  $\kappa_{PS}, \kappa_{VA}$ , and  $\kappa_{TX}$  in the first three rows of table 3.

In the second step, we extrapolate  $A(a)$  and  $B(a)$  to the continuum limit ( $a \rightarrow 0$ ). We consider both linear and exponential extrapolations in  $a^2$ :

$$f(a) = f_0 + f_1 a^2, \quad \text{or} \quad f(a) = f_0 \exp(f_1 a^2),$$

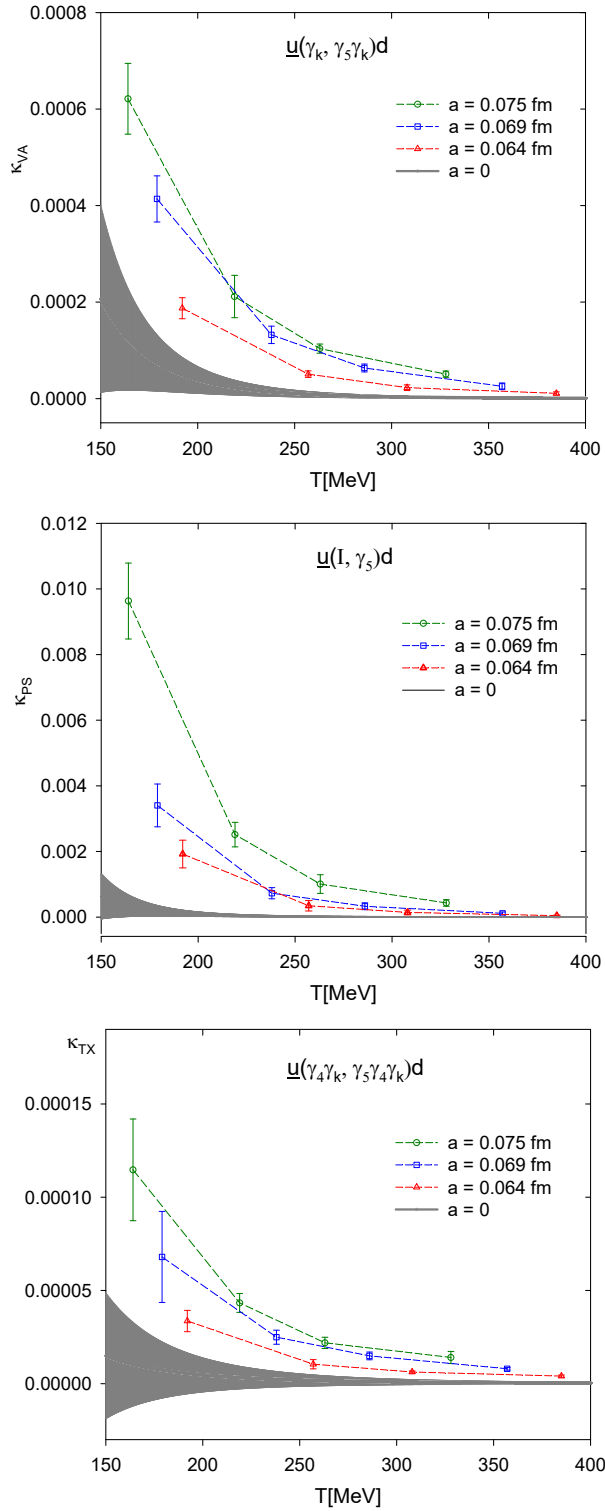


**Figure 3:** RG-invariant symmetry ratios  $\kappa_{VA}$  and  $\{\kappa_{PS}, \kappa_{TX}\}$  for the  $SU(2)_L \times SU(2)_R$  and  $U(1)_A$  chiral symmetries of  $(u, d)$  quarks, computed at three lattice spacings  $a = (0.075, 0.069, 0.064)$  fm and twelve temperatures in the range 164–385 MeV. The solid line and its band denote the continuum-extrapolated value and its uncertainty from 2D global fit.

$a$ [fm]	$\kappa_{PS}$			$\kappa_{VA}$			$\kappa_{TX}$		
	$A \times 10^7$	$B$	$\chi^2/\text{dof}$	$A \times 10^7$	$B$	$\chi^2/\text{dof}$	$A \times 10^7$	$B$	$\chi^2/\text{dof}$
0.064	2.4(1.9)	5.4(5)	0.04	1.5(9)	4.3(4)	0.19	1.0(2)	3.3(2)	0.18
0.069	6.3(5.2)	5.0(5)	0.13	4.2(1.9)	4.0(3)	0.01	4.1(1.1)	2.9(2)	0.32
0.075	25.0(14.1)	4.6(4)	0.11	8.1(2.9)	3.7(2)	0.21	5.0(3.9)	2.8(6)	0.24
2-step	$8.2(23.3) \times 10^{-3}$	7.5(1.9)	0.03, 0.01	$3.6(7.1) \times 10^{-2}$	5.9(1.4)	0.14, 0.01	$4.2(8.3) \times 10^{-3}$	5.2(1.2)	0.10, 0.28
2D	$1.8(5.5) \times 10^{-2}$	6.7(2.0)	0.31	$3.3(6.2) \times 10^{-2}$	5.8(1.3)	0.93	$7.3(16.0) \times 10^{-2}$	4.0(1.7)	1.16

**Table 3:** Fitted parameters  $A(a)$ ,  $B(a)$ , and  $\chi^2/\text{dof}$  for the power-law ansatz  $\kappa(a, T) = A(a)(T[\text{GeV}])^{-B(a)}$  for  $\kappa_{PS}$ ,  $\kappa_{VA}$ , and  $\kappa_{TX}$  at three lattice spacings. The last two rows present the continuum results ( $a = 0$ ) obtained via the two-step and 2D global fitting methods.

and choose between them based on the behavior of the data. If a linear fit yields an unphysical  $f_0 < 0$ , we adopt the exponential form, which includes higher-order contributions in  $a^2$  and ensures positivity of  $f_0$ . For cases where both forms are viable, we select the one that gives the better fit to the data. The requirement  $f_0 > 0$  is physically motivated:  $A_0 < 0$  would imply  $\kappa(a = 0, T) < 0$ , contradicting the definition  $\kappa_{AB} \geq 0$  from Eq. (2.18), while  $B_0 < 0$  would imply that  $\kappa$  increases with  $T$ , inconsistent with the expected decrease of  $SU(2)_L \times SU(2)_R$  and  $U(1)_A$  breakings as temperature rises. Based on this criterion, we use exponential extrapolation for  $A(a)$ , and linear extrapolation for  $B(a)$ ,

$$A(a) = A_0 \exp(A_1 a^2), \quad (5.2)$$

$$B(a) = B_0 + B_1 a^2. \quad (5.3)$$

The continuum-extrapolated parameters  $A_0$  and  $B_0$  of the two-step method, along with their  $\chi^2/\text{dof}$ , are listed for  $\kappa_{PS}$ ,  $\kappa_{VA}$ , and  $\kappa_{TX}$  in the second-to-last row of table 3.

Guided by the functional forms adopted in the two-step method, we also perform a simultaneous two-dimensional (2D) global fit to all 12 data points of each  $\kappa_{AB}(a, T)$  using the following model:

$$\kappa(a, T) = A_0 \exp(A_1 a^2) (T[\text{GeV}])^{-(B_0 + B_1 a^2)}. \quad (5.4)$$

The resulting continuum parameters  $A_0$  and  $B_0$  and the corresponding  $\chi^2/\text{dof}$  are given in the last row of table 3. For the two-step row, the two  $\chi^2/\text{dof}$  values correspond to the extrapolation of  $A(a)$  and  $B(a)$ , respectively. The values obtained from the 2D global fit are consistent with those from the two-step method.

Statistically, the 2D-fit is more reliable because it performs a simultaneous minimization over the entire dataset, which ensures a globally optimized balance between parameters  $A$  and  $B$ . In contrast, the 2-step fit first fits each  $a$ -group independently to obtain local estimates  $A(a)$  and  $B(a)$ , then performs a secondary regression on those results. This "fit-of-fits" approach propagates errors less efficiently and can introduce bias if a particular  $a$ -group exhibits larger statistical fluctuations.

We therefore adopt the 2D-fit results for  $A_0$  and  $B_0$  to obtain the continuum-extrapolated  $\kappa_{PS}$ ,  $\kappa_{VA}$ , and  $\kappa_{TX}$ . These are shown as solid curves in figure 3, with the error bands indicating the uncertainty. The continuum extrapolated values of  $\kappa_{PS}$ ,  $\kappa_{VA}$  and  $\kappa_{TX}$  are

$T[\text{MeV}]$	$\kappa_{PS}(a=0)$	$\kappa_{VA}(a=0)$	$\kappa_{TX}(a=0)$
150	$(6.3 \pm 6.8) \times 10^{-4}$	$(2.1 \pm 1.9) \times 10^{-4}$	$(1.5 \pm 4.2) \times 10^{-5}$
164	$(3.4 \pm 3.3) \times 10^{-4}$	$(1.2 \pm 1.1) \times 10^{-4}$	$(1.0 \pm 2.8) \times 10^{-5}$
179	$(1.9 \pm 1.5) \times 10^{-4}$	$(7.4 \pm 5.8) \times 10^{-5}$	$(7.3 \pm 19.1) \times 10^{-6}$
219	$(4.9 \pm 3.0) \times 10^{-5}$	$(2.3 \pm 1.5) \times 10^{-5}$	$(3.3 \pm 7.8) \times 10^{-6}$
257	$(1.7 \pm 1.1) \times 10^{-5}$	$(9.0 \pm 5.8) \times 10^{-6}$	$(1.7 \pm 3.8) \times 10^{-6}$
385	$(1.1 \pm 1.3) \times 10^{-6}$	$(8.5 \pm 7.2) \times 10^{-7}$	$(3.4 \pm 6.7) \times 10^{-7}$

**Table 4:** Continuum extrapolated values of  $\kappa_{PS}$ ,  $\kappa_{VA}$ , and  $\kappa_{TX}$  at selected temperatures between 150 and 400 MeV.

compatible with one another across the temperature range 150–400 MeV, within our precision. This is illustrated explicitly in table 4, which lists the continuum values at several representative temperatures.

## 6 Discussion and Outlook

In this work, we have introduced a renormalization-group invariant observable, the symmetry strength parameter  $\kappa_{AB}$ , designed to provide a quantitative and scheme-independent measure of symmetry breaking in QCD. Using this ratio, we have performed a systematic lattice study of the relative strength of  $SU(2)_L \times SU(2)_R$  chiral symmetry breaking and  $U(1)_A$  axial symmetry breaking in finite-temperature QCD with  $N_f = 2 + 1 + 1$  flavors, employing optimal domain-wall fermions at the physical point. Our analysis spans three lattice spacings and twelve temperatures in the range 164–385 MeV, allowing for controlled continuum extrapolations across the chiral crossover region.

We examined three independent symmetry-breaking channels in the *nonsinglet sector with quark-connected correlators*, namely: the scalar–pseudoscalar channel sensitive to  $U(1)_A$  breaking ( $\kappa_{PS}$ ), the vector–axial–vector channel probing chiral symmetry breaking ( $\kappa_{VA}$ ), and an additional  $U(1)_A$ -sensitive tensor–axial–tensor channel ( $\kappa_{TX}$ ). At finite lattice spacing, these channels exhibit a clear hierarchy:  $\kappa_{PS} > \kappa_{VA} > \kappa_{TX}$ . However, this hierarchy collapses in the continuum limit, where all three symmetry strength parameters become statistically indistinguishable within our current precision.

This degeneracy constitutes a robust, model-independent result obtained from a chirally symmetric lattice formulation and demonstrates that discretization effects play a central role in apparent differences among symmetry-breaking channels. From a physical perspective, our findings indicate that chiral and axial symmetry-breaking effects for the *nonsinglet* sector in QCD become comparably suppressed over a narrow temperature interval near the chiral crossover. We find no evidence for a parametrically separated restoration scale for  $U(1)_A$  symmetry relative to  $SU(2)_L \times SU(2)_R$  symmetry in the continuum limit—a result that places stringent quantitative constraints on phenomenological descriptions of finite-temperature QCD that rely on delayed axial symmetry restoration.

Within a renormalization-group framework, the observed continuum-limit degeneracy of  $\kappa_{PS}$ ,  $\kappa_{VA}$ , and  $\kappa_{TX}$  implies that  $SU(2)_L \times SU(2)_R$  and  $U(1)_A$  symmetry-breaking ef-

fects for *quark-connected correlators* become comparably suppressed near  $T_c$ . This suggests that the corresponding symmetry-breaking operators acquire similar infrared relevance for nonsinglet observables. However, as we discuss in section 6.1, the full effective restoration pattern—including singlet channels—reveals a more intricate structure that refines simple RG scenarios based solely on nonsinglet data.

### 6.1 Connections to topological susceptibility and singlet sector

An important subtlety involves the quark-disconnected parts of the scalar singlet ( $\sigma$ ) and pseudoscalar singlet ( $\eta$ ) mesons in  $N_f = 2$  QCD. Recall that the physical  $\eta'$  corresponds to the  $\eta$  singlet in  $N_f = 2$  QCD. Upon effective restoration of *full*  $SU(2)_L \times SU(2)_R$  chiral symmetry, i.e., satisfaction of equations (2.20)-(2.24), where (2.20) and (2.21) involving both nonsinglet and singlet channels yield

$$\chi_\sigma - \chi_\delta = \chi_\pi - \chi_\delta = \chi_\pi - \chi_\eta, \quad (6.1)$$

which relates the quark-disconnected parts of  $\chi_\sigma$  and  $\chi_\eta$ :

$$\chi_{\text{disc}} \equiv \chi_\sigma - \chi_\delta = \chi_\pi - \chi_\eta \equiv \chi_{5,\text{disc}}, \quad (6.2)$$

where

$$\chi_{\text{disc}} = \frac{1}{V} \left\{ \langle [\text{Tr}(D_c + m_q)^{-1}]^2 \rangle - \langle \text{Tr}(D_c + m_q)^{-1} \rangle^2 \right\}, \quad (6.3)$$

$$\chi_{5,\text{disc}} = \frac{1}{V} \left\{ \langle [\text{Tr}\gamma_5(D_c + m_q)^{-1}]^2 \rangle - \langle \text{Tr}\gamma_5(D_c + m_q)^{-1} \rangle^2 \right\}. \quad (6.4)$$

In lattice QCD with exact chiral symmetry, the topological charge  $Q_t$  satisfies

$$Q_t = m_q \text{Tr}\gamma_5(D_c + m_q)^{-1}, \quad \forall m_q > 0. \quad (6.5)$$

Assuming Eq. (6.5) can be measured precisely (e.g., with overlap fermions via index theorem), Eq. (6.2) implies

$$\chi_{\text{disc}} = \chi_{5,\text{disc}} = \frac{\chi_t}{m_q^2}, \quad (6.6)$$

where  $\chi_t$  is the topological susceptibility,

$$\chi_t = \frac{1}{V} (\langle Q_t^2 \rangle - \langle Q_t \rangle^2). \quad (6.7)$$

Thus, upon effective restoration of *full*  $SU(2)_L \times SU(2)_R$  chiral symmetry,  $\chi_t/m_q^2$  equals any of the three differences:  $\chi_\sigma - \chi_\delta$ ,  $\chi_\pi - \chi_\delta$ , or  $\chi_\pi - \chi_\eta$ . However, Eq. (6.1) presents a puzzle: how could  $(\chi_\pi - \chi_\delta)$ , which involves only quark-connected correlators, equal  $\chi_{\text{disc}} = \chi_t/m_q^2$ , which arises solely from quark-disconnected diagrams? This puzzle is resolved by considering the effective restoration of *full*  $U(1)_A$  axial symmetry, which requires both Eq. (2.25) (nonsinglet) and Eq. (2.26) (singlet) to be satisfied. Subtracting Eq. (2.25) from Eq. (2.26) gives

$$\chi_\sigma - \chi_\delta = \chi_\eta - \chi_\pi, \quad (6.8)$$

which contradicts Eq. (6.1) unless all susceptibility differences in both equations vanish—implying  $\chi_t = 0$ . In other words, *full* effective restoration of both  $SU(2)_L \times SU(2)_R$  and  $U(1)_A$  symmetries requires vanishing topological susceptibility.

This leads to a natural *two-stage hierarchical effective restoration* scenario illustrated in Fig. 4:

- **Stage 1** ( $T \sim T_c^{ns} \simeq T_c \sim 156$  MeV): Effective restoration of both  $SU(2)_L \times SU(2)_R$  and  $U(1)_A$  symmetries in the *nonsinglet* sector, where quark-connected correlators become degenerate:

$$- U(1)_A: \chi_\pi \approx \chi_\delta \text{ (Eq. 2.25), } \chi_{\rho_T} \approx \chi_{b_1} \text{ (eq. 2.27)}$$

$$- SU(2)_L \times SU(2)_R: \chi_\rho \approx \chi_{a_1} \text{ (eq. 2.24)}$$

- **Stage 2** ( $T \sim T_c^s \gg T_c^{ns}$ ): Full effective restoration including *singlet* and *mixed singlet-nonsinglet* channels, requiring  $\chi_t \rightarrow 0$ ,  $\kappa_{\omega_T, h_{1T}} \rightarrow 0$  and satisfaction of all relations (eqs. (2.20)–(2.28)) including eqs. (6.1) and (6.8):

$$- SU(2)_L \times SU(2)_R: \chi_\sigma = \chi_\pi, \chi_\eta = \chi_\delta, \chi_{\omega_T} = \chi_{b_1}, \chi_{h_{1T}} = \chi_{\rho_T}$$

$$- U(1)_A: \chi_\sigma = \chi_\eta, \chi_{\omega_T} = \chi_{h_{1T}}$$

In this picture,  $\chi_\pi - \chi_\delta$  (probing nonsinglet  $U(1)_A$  restoration) is distinct from  $\chi_\sigma - \chi_\delta$  and  $\chi_\pi - \chi_\eta$  (probing mixed singlet-nonsinglet channel restoration). The former can approach zero while the latter remain finite, reflecting the persistence of topological fluctuations. The key insight is that *both*  $SU(2)_L \times SU(2)_R$  and  $U(1)_A$  symmetries exhibit *two-stage restoration*: they first restore in the nonsinglet sector around  $T_c^{ns} \sim 156$  MeV, and only later restore fully (including singlet channels) at a much higher temperature  $T_c^s \gg T_c^{ns}$  when topological fluctuations are largely suppressed ( $\chi_t \rightarrow 0$ ).

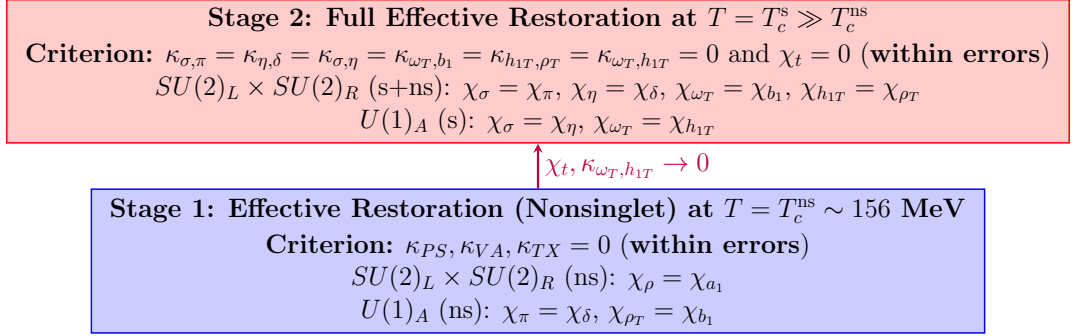
## 6.2 Hierarchical restoration of chiral and axial symmetries

Our analysis of  $\kappa_{PS}$ ,  $\kappa_{VA}$ , and  $\kappa_{TX}$  provides direct evidence for Stage 1 (nonsinglet restoration) of this hierarchical restoration. The near-vanishing of  $\kappa_{PS}$  and  $\kappa_{TX}$  around  $T_c$  demonstrates that  $U(1)_A$ -anomaly effects on *quark-connected correlators* become negligible in this regime, signaling effective  $U(1)_A$  restoration in the nonsinglet sector. Similarly,  $\kappa_{VA} \rightarrow 0$  indicates effective  $SU(2)_L \times SU(2)_R$  restoration in the nonsinglet sector.

This hierarchical picture explains the apparent tension between different lattice studies. In the nonsinglet sector ( $T \sim T_c^{ns} \sim 156$  MeV), both  $SU(2)_L \times SU(2)_R$  and  $U(1)_A$  symmetries effectively restore for quark-connected channels as thermal screening reduces instanton effects on chiral partner splittings ( $\pi$ - $\delta$ ,  $\rho$ - $a_1$ ,  $\rho_T$ - $b_1$ ). Conversely, full effective restoration ( $T \sim T_c^s \gg T_c^{ns}$ ) including singlet channels requires each of  $\kappa_{\sigma, \pi}$ ,  $\kappa_{\eta, \delta}$ ,  $\kappa_{\omega_T, b_1}$ ,  $\kappa_{h_{1T}, \rho_T}$ ,  $\kappa_{\sigma, \eta}$ , and  $\kappa_{\omega_T, h_{1T}}$  to go to zero, and  $\chi_t \rightarrow 0$ , which occur at significantly higher temperatures than  $T_c^{ns}$ .

For  $N_f = 2+1+1$  QCD at the physical point, the chiral transition is a smooth crossover. Consequently,  $\chi_\sigma - \chi_\delta$  or  $\chi_\eta - \chi_\pi$  never vanishes identically but gradually diminishes as  $T$  increases above  $T_c \sim T_c^{ns}$ . The relation  $\chi_\sigma - \chi_\delta = \chi_t/m_q^2$  is obscured in practice by

## Two-Stage Hierarchical Restoration (Effective)



**Temperature scale:**  $T_c^{ns} \sim 156$  MeV (Stage 1)  $\longrightarrow$   $T_c^s \gg T_c^{ns}$  (Stage 2, threshold-dependent)

### Observables (RG-invariant $\kappa_{AB}$ in the continuum limit):

$\kappa_{VA}$ :  $\rho$ - $a_1$  (nonsinglet  $SU(2)_L \times SU(2)_R$ , vector, connected)

$\kappa_{PS}$ :  $\pi$ - $\delta$  (nonsinglet  $U(1)_A$ , scalar, connected)

$\kappa_{TX}$ :  $\rho_T$ - $b_1$  (nonsinglet  $U(1)_A$ , tensor, connected)

$\kappa_{\sigma,\pi}$  (singlet-nonsinglet  $SU(2)_L \times SU(2)_R$ , scalar, **Stage 2 probe**)

$\kappa_{\eta,\delta}$  (singlet-nonsinglet  $SU(2)_L \times SU(2)_R$ , scalar, **Stage 2 probe**)

$\kappa_{\omega_T,b_1}$  (singlet-nonsinglet  $SU(2)_L \times SU(2)_R$ , tensor, **Stage 2 probe**)

$\kappa_{h_{1T},\rho_T}$  (singlet-nonsinglet  $SU(2)_L \times SU(2)_R$ , tensor, **Stage 2 probe**)

$\kappa_{\sigma,\eta}$  (singlet  $U(1)_A$ , scalar, **Stage 2 probe**)

$\kappa_{\omega_T,h_{1T}}$  (singlet  $U(1)_A$ , tensor, **Stage 2 probe**)

$\chi_t$ : topological susceptibility (**Stage 2 probe**)

*Neither stage implies exact restoration; both are operational thresholds defined by  $\kappa_{AB} = 0$  within errors.*

**Figure 4:** Schematic illustration of the two-stage hierarchical restoration scenario for light ( $u, d$ ) quarks. Stage 1 (nonsinglet restoration) occurs around  $T_c^{ns} \sim 156$  MeV, while Stage 2 (full effective restoration including singlets) occurs at a much higher temperature  $T_c^s \gg T_c^{ns}$ . The  $\kappa_{AB}$  ratios for nonsinglet channels ( $\kappa_{PS}, \kappa_{VA}, \kappa_{TX}$ ) probe Stage 1, while singlet and mixed singlet-nonsinglet ratios  $\kappa(\sigma, \pi)$ ,  $\kappa(\eta, \delta)$ ,  $\kappa(\omega_T, b_1)$ ,  $\kappa(h_{1T}, \rho_T)$ ,  $\kappa(\sigma, \eta)$ ,  $\kappa(\omega_T, h_{1T})$ , and direct  $\chi_t$  measurements probe Stage 2.

lattice artifacts, residual chiral symmetry breaking, and the inherent nonzero difference in a crossover. Lattice determinations of  $\chi_t(T)$  suffer from significant discretization artifacts, and a consistent continuum picture has not yet emerged across different studies (see e.g., [46, 52–55]). In general, for  $N_f = 2 + 1$  and  $N_f = 2 + 1 + 1$  QCD at physical masses,  $\chi_t(T)$  remains sizeable up to  $T \gg T_c$ , indicating that topological fluctuations are not fully suppressed until well above the chiral crossover.

Notably, in lattice QCD with exact chiral symmetry,  $\chi_t(T)$  for physical  $N_f = 2 + 1$  and  $N_f = 2 + 1 + 1$  QCD can be much larger than that of  $N_f = 2$  QCD in the chiral limit (see appendix A of ref. [56]). This raises an intriguing possibility: in the  $N_f = 2$  chiral limit, the two-stage hierarchy might nearly collapse, with  $T_c^s \gtrsim T_c^{ns} \sim T_c$ , implying that full effective restoration (including singlet channels) could occur much closer to the chiral transition

temperature. Our simulations at physical masses cannot address this scenario directly, as the strange and charm quarks explicitly break the symmetry and enhance topological fluctuations.

Our  $\kappa_{PS}$ ,  $\kappa_{VA}$ , and  $\kappa_{TX}$  measurements, being ratios, cancel many systematics and cleanly show the trend toward symmetry restoration in the nonsinglet sector. The persistence of  $\chi_t > 0$  for  $T \gtrsim T_c$  in lattice studies is therefore not in tension with  $\kappa_{PS}, \kappa_{VA}, \kappa_{TX} \rightarrow 0$ ; rather, it reflects the hierarchy  $T_c^{ns} \approx T_c < T_c^s$ . The anomaly thus influences different observables in distinct ways and on different temperature scales. While  $\chi_t$  probes the global topological charge distribution and remains finite until much higher temperatures (falling off with a power-law consistent with dilute instanton gas prediction [57], although the overall normalization may differ significantly), nonsinglet meson correlators are sensitive primarily to the *anomaly-induced splitting* within chiral partners—a splitting that can diminish due to thermal screening even while topological fluctuations themselves persist.

**Probing full effective restoration with singlet channels** While  $\kappa_{PS}$ ,  $\kappa_{VA}$ , and  $\kappa_{TX}$  cleanly signal nonsinglet restoration near  $T_c^{ns}$ , establishing Stage 2 requires probing six additional channels that involve singlet operators. Four of these probe  $SU(2)_L \times SU(2)_R$  restoration between singlet and nonsinglet partners:  $\kappa_{\sigma,\pi}$ ,  $\kappa_{\eta,\delta}$ ,  $\kappa_{\omega_T,b_1}$  and  $\kappa_{h_{1T},\rho_T}$ . Two probe  $U(1)_A$  restoration in the singlet sector:  $\kappa_{\sigma,\eta}$  and  $\kappa_{\omega_T,h_{1T}}$ . All six are RG-invariant (section 2.2), and all require quark-disconnected diagrams — the dominant computational challenge. The only additional complication arises for channels involving the scalar singlet  $\sigma$ , which requires VEV subtraction. If the hierarchical picture is correct, all six ratios should remain non-zero well above  $T_c^{ns}$  and approach zero only at a higher temperature  $T_c^s \gg T_c^{ns}$ .

### 6.3 Broader symmetry landscape and emergent phases above $T_c$

The hierarchical picture presented above aligns with growing evidence for multi-stage transitions above  $T_c$ . Beyond the familiar  $SU(2)_L \times SU(2)_R$  and  $U(1)_A$  symmetries, recent lattice studies reveal emergent approximate symmetries absent in the classical QCD Lagrangian. In particular, approximate chiral-spin  $SU(2)_{CS}$  symmetry [58] observed in  $N_f = 2$  [59, 60],  $N_f = 2 + 1 + 1$  [25, 32], and  $N_f = 2 + 1 + 1 + 1$  [33] lattice QCD indicates that hadron-like states bound predominantly by chromoelectric interactions persist well above  $T_c$ .

It is important to distinguish this emergent symmetry from the usual chiral symmetries. For  $SU(2)_L \times SU(2)_R$  and  $U(1)_A$ , symmetry breaking decreases monotonically with temperature, and the symmetries themselves become effectively restored as partner degeneracy improves. These symmetries are always present in the Lagrangian — only their breaking weakens.

In contrast,  $SU(2)_{CS}$  chiral-spin symmetry is not present in the QCD Lagrangian. It emerges only in an intermediate window where chromoelectric binding dominates, typically from  $T \sim 2T_c$  up to  $T \sim 4T_c$  for light ( $u, d$ ) quarks. The window boundaries depend on two thresholds:  $\epsilon_{CS}$  for emergence at  $T_{CS}$ , and  $\epsilon_{CSF}$  for fading at  $T_{CSF} > T_{CS}$ . Within this window,  $SU(2)_{CS}$  breaking decreases with  $T$ , allowing hadron-like states bound by chromoelectric interactions to exist. As temperature increases, thermal excitation energy

eventually exceeds the chromoelectric binding energy, leading to quark deconfinement. This is manifested when one  $SU(2)_{\text{CS}}$  multiplet  $(V_k, T_k, X_k)$  merges with the  $(P, S)$  multiplet of  $U(1)_A$  symmetry, leaving only the usual chiral symmetries relevant. At this point, chiral-spin symmetry *fades away* — not simply becoming more broken, but physically disappearing due to thermal excitations.

Similarly, the observation of an infrared symmetric phase [61] around  $T_{\text{IR}} \sim 230$  MeV in  $N_f = 2 + 1$  lattice QCD [62], which disappears by  $T \gtrsim 300$  MeV, supports a correlated, quasi-hadronic medium in the window  $T_c \lesssim T \lesssim 2T_c$ . In this regime, hadrons become progressively delocalized, forming a dense fluid where both chromoelectric and chromomagnetic interactions remain active. The usual chiral multiplets are already restored in the nonsinglet sector, but chiral-spin symmetry is not yet manifest.

The gradual loss of binding across both regimes is consistent with the observed reduction in  $U(1)_A$ -breaking effects in quark-connected channels (as measured by  $\kappa_{PS}$  and  $\kappa_{TX}$ ), while topological fluctuations—including center vortices [63] and instanton-like objects—remain active until higher temperatures.

These emergent symmetry patterns are complemented by topological studies. Center-vortex analyses in  $N_f = 2 + 1$  QCD observe a pronounced change in vortex percolation at approximately  $\gtrsim 2T_c$  [64]. While vortex density drops substantially, a sparse network survives to higher temperatures, reinforcing that topological fluctuations — intimately connected to the  $U(1)_A$  anomaly — remain non-negligible well into the deconfined regime. This provides a plausible mechanism for continued  $U(1)_A$  breaking where nonsinglet chiral symmetry is largely restored. The smooth crossover implies no sharp “complete deconfinement” point; instead, the system evolves gradually from hadronic to quark–gluon plasma, with residual correlations possible even at  $T \gg 2T_c$ .

Taken together, these independent lines of evidence support the two-stage effective restoration scenario described in section 6.1. Stage 1 ( $T \sim T_c^{ns}$ ) is characterized by effective restoration of nonsinglet symmetries, as demonstrated by the vanishing of  $\kappa_{PS}$ ,  $\kappa_{VA}$ , and  $\kappa_{TX}$  in this work. Stage 2 ( $T \sim T_c^s$ ) involves full effective restoration of singlet channels and suppression of topological fluctuations ( $\chi_t \rightarrow 0$ ). Consistent comparison between lattice studies requires continuum extrapolation of each observable, as demonstrated here. Since the chiral transition at physical quark masses is a smooth crossover, any symmetry-breaking observable decreases gradually with temperature. The Stage 2 scenario remains to be conclusively established through future continuum-extrapolated measurements of tensor-singlet ratios and topological susceptibility.

#### 6.4 Future computational improvements and extensions

To build upon this work, several improvements are planned:

- **Nonsinglet channels:** Simulations at several fixed temperatures, each with multiple lattice spacings and larger spatial volumes ( $40^3$  and  $64^3$ ), to reduce systematic uncertainties in the continuum extrapolation of  $\kappa_{PS}$ ,  $\kappa_{VA}$ , and  $\kappa_{TX}$ .
- **Singlet channels:** Using stochastic all-to-all propagators with color–Dirac dilution to handle the computationally demanding quark-disconnected diagrams, we will com-

pute the six singlet-involving ratios identified above ( $\kappa_{\sigma,\pi}$ ,  $\kappa_{\eta,\delta}$ ,  $\kappa_{\omega_T,b_1}$ ,  $\kappa_{h_{1T},\rho_T}$ ,  $\kappa_{\sigma,\eta}$ ,  $\kappa_{\omega_T,h_{1T}}$ ), enabling a direct test of the two-stage restoration scenario.

- **Topological susceptibility:** Direct measurements of  $\chi_t$  using the overlap operator and index theorem will complement the  $\kappa_{AB}$  ratios and comprehensively map the symmetry restoration landscape.

## 6.5 RG interpretation and comparison with Pisarski–Wilczek analyses

The renormalization-group analysis of Pisarski and Wilczek (PW) [14] shows that the order of the two-flavor chiral transition is controlled by the RG scaling of the  $U(1)_A$ -breaking operator at the  $O(4)$  fixed point. If this operator is *relevant*, the  $U(1)_A$ -breaking perturbation grows under RG flow and the infrared physics is governed by the stable  $O(4)$  Wilson–Fisher fixed point, allowing a *second-order transition in the  $O(4)$  universality class*. If it is *irrelevant*, the perturbation flows to zero and the effective symmetry enlarges to  $U(2)_L \times U(2)_R$ ; the  $\epsilon$ -expansion of the corresponding Landau–Ginzburg theory reveals *no infrared-stable fixed point*, implying runaway RG flow and a *fluctuation-induced first-order transition*. The subsequent analysis of Pelissetto and Vicari (PV) [65] established that for  $N_f = 2$  this operator is *marginally irrelevant* at the  $O(4)$  fixed point, implying approximate  $O(4)$  scaling in the chiral limit near the PW critical temperature.

The PW/PV scenario applies strictly to the *chiral limit* ( $m_q = 0$ ) at the exact infrared critical fixed point and therefore characterizes *universality classes*, rather than specific observables at finite quark mass. In physical QCD with  $m_q \neq 0$ , where the transition is a smooth crossover and no true critical fixed point exists, axial symmetry restoration must be defined operationally. In this work, we define “effective restoration” through the vanishing of the  $\kappa_{AB}$  ratio within statistical uncertainties (section 2.3). This condition is substantially weaker than the RG irrelevance criterion of PW: it does not imply enlargement of the symmetry to  $U(2)_L \times U(2)_R$  or a change in universality class, but only that symmetry-breaking effects are not resolved within the present observables and statistical precision.

With this distinction, our results reveal a **two-stage pattern of operational symmetry restoration** that differs qualitatively from the single-scale PW/PV scenario.

**Stage 1 (nonsinglet sector):** Near  $T_c^{\text{ns}} \sim 156$  MeV, the ratios  $\kappa_{PS}$ ,  $\kappa_{VA}$ , and  $\kappa_{TX}$  become consistent with zero, indicating operational effective restoration of  $SU(2)_L \times SU(2)_R$  and  $U(1)_A$  in the nonsinglet sector. However, this temperature does not correspond to the critical temperature of the PW framework, which refers to the chiral limit and requires restoration of full chiral symmetry at the infrared fixed point. Since singlet channels remain nondegenerate, the universality-class arguments of PW do not directly apply at this stage.

**Stage 2 (singlet sector):** At a significantly higher temperature  $T_c^{\text{s}} \gg T_c^{\text{ns}}$ , the singlet-involving ratios  $\kappa_{\sigma,\eta}$ ,  $\kappa_{\omega_T,h_{1T}}$ ,  $\kappa_{\sigma,\pi}$ ,  $\kappa_{\eta,\delta}$ ,  $\kappa_{\omega_T,b_1}$ , and  $\kappa_{h_{1T},\rho_T}$ , and the topological susceptibility  $\chi_t$  also become consistent with zero, extending operational effective restoration to both singlet and nonsinglet sectors. This defines a more complete restoration scale than the PW critical temperature, which is determined solely by chiral symmetry in the massless limit and does not require observable axial degeneracy. Nevertheless, even at  $T_c^{\text{s}}$ , this operational restoration does not by itself establish enlargement of the symmetry to

$U(2)_L \times U(2)_R$  or determine the universality class, as explicit symmetry-breaking effects from finite quark masses and the anomaly remain present in the Lagrangian. Rather,  $T_c^s$  marks the temperature at which symmetry breaking becomes unresolvable in all measured channels, representing a stronger phenomenological restoration scale beyond the strict RG definition of criticality.

This two-stage hierarchy does not follow from the PW/PV fixed-point analysis, which applies strictly in the chiral limit and does not distinguish quark-connected and quark-disconnected contributions. Our temperatures  $T_c^{\text{ns}}$  and  $T_c^s$  are crossover scales in physical QCD rather than critical points, and the persistence of  $\chi_t > 0$  reflects the continued contribution of quark-disconnected diagrams and the mass-dependent amplification of axial-anomaly effects. Thus, while marginal irrelevance provides an important conceptual backdrop, the hierarchical restoration observed here represents a distinct finite-mass phenomenon beyond the scope of the chiral-limit RG framework.

This interpretation is supported by complementary lattice studies probing chiral symmetry restoration from different perspectives. In the  $N_f = 2$  chiral limit, continuum-controlled simulations using a many-flavor approach find that the apparent first-order behavior on coarse lattices is a discretization artifact, with the continuum transition consistent with second order and compatible with  $O(N)$  scaling [66]. At the physical point in  $N_f = 2 + 1 + 1$  QCD, independent scaling analysis with twisted-mass Wilson fermions [67] shows quantitative agreement with 3D  $O(4)$  scaling over a broad temperature range, indicating that approximate critical scaling emerges already at nonzero quark mass.

Within this framework, our  $\kappa_{AB}$  observables provide the first continuum-extrapolated, quantitative evidence for **Stage 1**, namely the operational restoration of  $SU(2)_L \times SU(2)_R$  and  $U(1)_A$  in the nonsinglet (quark-connected) sector near  $T_c$ . It is worth noting that other ratios such as  $\kappa_{\sigma,\pi}$  and  $\kappa_{\eta,\delta}$ , which involve singlet channels, are also formally RG-invariant, as the underlying renormalization constants satisfy  $Z_S^{\text{ns}} = Z_P^{\text{ns}} = Z_S^s = Z_P^s$  (see section 2.2). However, in practice, the singlet susceptibilities involve additional complications:  $\chi_\eta$  is connected to  $\chi_t$  through the exact relation  $\chi_\pi - \chi_{\eta'} = \chi_t/m_q^2$  (eq. 6.6), while  $\chi_\sigma$  requires subtraction of quark-disconnected contributions that are computationally demanding. These difficulties, together with the noise from quark-disconnected diagrams, make these ratios less accessible in the present study.

Together, these results support a coherent picture in which the axial anomaly becomes progressively less visible near the chiral crossover. The chiral-limit studies establish the relevance of  $O(N)$ -type critical behavior at the true fixed point, while physical-mass simulations demonstrate that approximate  $O(4)$ -like scaling and chiral partner degeneracy appear as precursor phenomena. Our observation of nonsinglet degeneracy near  $T_c^{\text{ns}}$  is consistent with this framework, while the delayed restoration in singlet channels reveals additional finite-mass and anomaly-driven effects beyond the strict chiral-limit universality-class description.

Functional renormalization-group analyses of  $(2 + 1)$ -flavor QCD [68] similarly find that axial-anomaly effects persist throughout a broad crossover region. While nonsinglet observables exhibit degeneracy patterns consistent with approximate  $O(4)$ -like symmetry, singlet channels remain sensitive to anomaly-driven quark-disconnected contributions. As a result, the fully symmetric  $U(2)_L \times U(2)_R$  scenario—requiring both  $m_q = 0$  and exact

irrelevance of axial breaking at the infrared fixed point—is not realized at the physical crossover temperature and is therefore not directly applicable to our simulation. Instead, the system follows a hierarchical restoration pattern consistent with our two-stage picture.

Establishing **Stage 2**, corresponding to full operational restoration including singlet channels, requires each of  $\kappa_{\sigma,\eta}$ ,  $\kappa_{\omega_T,h_{1T}}$ ,  $\kappa_{\sigma,\pi}$ ,  $\kappa_{\eta,\delta}$ ,  $\kappa_{\omega_T,b_1}$ , and  $\kappa_{h_{1T},\rho_T}$  to go to zero, and  $\chi_t \rightarrow 0$  within uncertainties. Existing lattice studies show that topological fluctuations persist up to  $T \gtrsim 2T_c$  (see e.g., [46, 52–55]), indicating that anomaly effects remain active well above the crossover. However, a definitive continuum-limit determination combining chirally symmetric fermions and overlap-based topology measurements for both sea and valence sectors is still lacking. Such calculations are necessary to determine whether and at what temperature full effective restoration occurs.

Importantly, our results do not contradict the PW/PV analysis, but instead probe a different regime. The observed degeneracy of nonsinglet chiral partners near  $T_c$  is a necessary precursor for  $O(4)$ -like scaling, but does not by itself establish the associated universality class. The behavior of the singlet sector—and whether its eventual operational restoration at  $T_c^s$  bears any connection to the  $U(2)_L \times U(2)_R$  scenario considered in the chiral-limit analysis—remains an open question. Future continuum-extrapolated measurements of  $\kappa_{\sigma,\eta}$  and  $\kappa_{\omega_T,h_{1T}}$  will directly probe the anomaly’s role in the singlet sector and further constrain the underlying symmetry-restoration mechanism.

## 6.6 Concluding remarks

The symmetry-strength parameter  $\kappa_{AB}$  introduced here provides a flexible and systematically improvable framework for quantifying symmetry breaking in QCD. Applied to finite-temperature QCD, it leads to several central conclusions:

1. **RG-invariant diagnostics:** The  $\kappa_{AB}$  ratios furnish renormalization-group invariant, scheme-independent measures of symmetry breaking across different operator channels, allowing direct comparison between lattice spacings and formulations.
2. **Continuum convergence:** Although finite- $a$  effects produce channel-dependent hierarchies, all nonsinglet  $\kappa_{AB}$  values converge consistently in the continuum limit, indicating a common restoration scale for different manifestations of chiral and axial symmetry in the quark-connected sector.
3. **Hierarchical restoration:** Both  $SU(2)_L \times SU(2)_R$  and  $U(1)_A$  exhibit a two-stage restoration pattern in the crossover regime: first in the nonsinglet sector around  $T_c^{\text{ns}} \sim 156$  MeV, and only at significantly higher temperature in the singlet sector, where suppression of topological fluctuations ( $\chi_t \rightarrow 0$ ) becomes essential. Six singlet-involving  $\kappa_{AB}$  ratios (two for  $U(1)_A$ :  $\kappa_{\sigma,\eta}$ ,  $\kappa_{\omega_T,h_{1T}}$ ; four for  $SU(2)_L \times SU(2)_R$ :  $\kappa_{\sigma,\pi}$ ,  $\kappa_{\eta,\delta}$ ,  $\kappa_{\omega_T,b_1}$ ,  $\kappa_{h_{1T},\rho_T}$ ) provide direct probes of this second stage, complementing direct measurements of  $\chi_t$ .

Natural extensions include simulations at lighter quark masses to probe scaling behavior more directly, applications to additional operator and flavor sectors, and systematic comparison with functional renormalization-group and effective-model studies. More broadly,

the  $\kappa_{AB}$  program establishes a quantitative benchmark for assessing symmetry realization in QCD and clarifies the relation between lattice observables and continuum effective descriptions of the chiral transition.

Combined with future continuum-extrapolated determinations of tensor singlet channels and overlap-fermion-based measurements of  $\chi_t$ , this framework offers a comprehensive strategy for mapping the complete restoration pattern of chiral and axial symmetries in QCD.

## A Meson Operator Notation

**Table 5:** Summary of meson operators and their corresponding regularized susceptibilities in  $N_f = 2$  QCD. The notation follows eqs. (2.20)–(2.28) in the main text. Singlet ( $s$ ) and nonsinglet ( $ns$ ) channels are distinguished, with the latter involving only quark-connected diagrams. Tensor operators  $T_k$  and  $X_k$  ( $k = 1, 2, 3$ ) are defined with spatial index  $k$ .

Meson	Operator	Channel	Flavor	Susceptibility
$\pi^a$	$\bar{q}\gamma_5 t^a q$	Pseudoscalar ( $P$ )	Nonsinglet ( $ns$ )	$\chi_\pi = \chi_P^{ns}$
$\delta^a$	$\bar{q}t^a q$	Scalar ( $S$ )	Nonsinglet ( $ns$ )	$\chi_\delta = \chi_S^{ns}$
$\sigma$	$\bar{q}q$	Scalar ( $S$ )	Singlet ( $s$ )	$\chi_\sigma = \chi_S^s$
$\eta$ ( $N_f = 2$ )	$\bar{q}\gamma_5 q$	Pseudoscalar ( $P$ )	Singlet ( $s$ )	$\chi_\eta = \chi_P^s$
$\rho^a$	$\bar{q}\gamma_i t^a q$	Vector ( $V_i$ )	Nonsinglet ( $ns$ )	$\chi_\rho = \chi_{V_i}^{ns}$
$a_1^a$	$\bar{q}\gamma_5 \gamma_i t^a q$	Axial-vector ( $A_i$ )	Nonsinglet ( $ns$ )	$\chi_{a_1} = \chi_{A_i}^{ns}$
$\omega$	$\bar{q}\gamma_i q$	Vector ( $V_i$ )	Singlet ( $s$ )	$\chi_\omega = \chi_{V_i}^s$
$h_1$	$\bar{q}\gamma_5 \gamma_i q$	Axial-vector ( $A_i$ )	Singlet ( $s$ )	$\chi_{h_1} = \chi_{A_i}^s$
$\rho_T^a$	$\bar{q}\gamma_4 \gamma_i t^a q$	Tensor ( $T_i$ )	Nonsinglet ( $ns$ )	$\chi_{\rho_T} = \chi_{T_i}^{ns}$
$b_1^a$	$\bar{q}\gamma_5 \gamma_4 \gamma_i t^a q$	Axial-tensor ( $X_i$ )	Nonsinglet ( $ns$ )	$\chi_{b_1} = \chi_{X_i}^{ns}$
$\omega_T$	$\bar{q}\gamma_4 \gamma_i q$	Tensor ( $T_i$ )	Singlet ( $s$ )	$\chi_{\omega_T} = \chi_{T_i}^s$
$h_{1T}$	$\bar{q}\gamma_5 \gamma_4 \gamma_i q$	Axial-tensor ( $X_i$ )	Singlet ( $s$ )	$\chi_{h_{1T}} = \chi_{X_i}^s$

- For  $N_f = 2$  flavor, the generators are  $t^0 = \mathbf{1}/2$  (for flavor singlet) and  $t^a = \tau^a/2$  ( $a = 1, 2, 3$  for flavor nonsinglets), where  $\mathbf{1}$  is the  $2 \times 2$  identity matrix and  $\tau^a$  are the Pauli matrices. They satisfy the normalization condition  $\text{tr}(t^a t^b) = \delta^{ab}/2$  for all  $a, b = 0, 1, 2, 3$ .
- The flavor-singlet generator  $t^0$  is always suppressed in our notation for singlet operators; e.g., we write  $\bar{q}q$  to mean  $\bar{q}t^0 q$ , and similarly  $\bar{q}\gamma_5 q$  for  $\bar{q}\gamma_5 t^0 q$ .
- Spatial index  $i = 1, 2, 3$  (or  $k = 1, 2, 3$ ) is implicit for vector and tensor channels.
- Singlet operators ( $\sigma, \eta, \omega, h_1, \omega_T, h_{1T}$ ) involve quark-disconnected diagrams and require VEV subtraction (for  $\sigma$ ) or disentanglement from  $\chi_t$  (for  $\eta$ ); see section 2.4.
- Nonsinglet operators involve only quark-connected diagrams and have cleaner renormalization properties.
- The tensor representations  $\rho_T^a$  (via  $T_i$ ) and  $b_1^a$  (via  $X_i$ ) probe  $U(1)_A$  through a different Dirac structure than the scalar–pseudoscalar pair ( $\delta$ – $\pi$ ).
- The vector singlet  $\omega$  and axial-vector singlet  $h_1$  are *not*  $U(1)_A$  partners, since both currents are invariant under  $U(1)_A$  ( $\{\gamma_5, \gamma_\mu\} = 0$ ). In contrast, the tensor singlet  $\omega_T$  and axial-tensor singlet  $h_{1T}$  are  $U(1)_A$  partners ( $\{\gamma_5, \gamma_4 \gamma_k\} \neq 0$ ), analogous to the scalar–pseudoscalar pair in the tensor channel.

## B Tables of results

In this appendix, we provide numerical data of the figures in the main text. Specifically, the data for the time-correlation functions, bare susceptibilities at the reference temperature, regularized susceptibilities, and RG-invariant symmetry ratios for  $u, d$  off-diagonal flavor-nonsinglet mesons are presented in tabular form.

The numerical values for the time-correlation functions  $C_\Gamma(t)$  of the  $\bar{u}\Gamma d$  on the  $32^3 \times 16$  lattice, shown in figure 1, are tabulated in tables 6–8 for the ( $P, S, V, A, T, X$ ) channels, for three lattice spacings  $a = (0.075, 0.069, 0.064)$  fm.

Numerical results for the bare susceptibilities (3.3) ( $\chi_S, \chi_P, \chi_V, \chi_A, \chi_T, \chi_X$ ) at the reference temperature  $aT_r = 1/4$  are listed in table 9.

Numerical results for the regularized susceptibilities (3.4) ( $\chi_S, \chi_P, \chi_V, \chi_A, \chi_T, \chi_X$ ), presented in figure 2, are listed in tables 10–12. These tables also include the corresponding RG-invariant symmetry ratios  $\kappa_{PS}, \kappa_{VA}$ , and  $\kappa_{TX}$ , shown in figure 3. Data are provided for the same three lattice spacings across twelve temperatures ranging from 164 to 385 MeV.

Statistical uncertainties are estimated using the jackknife method with a bin size of 5–15 configurations of which the statistical error saturates. The numerical values are quoted with more significant figures than strictly warranted by the precision. This choice is intentional, to clearly resolve subtle differences—particularly between symmetry partners such as  $\chi_V$  and  $\chi_A$ —that might otherwise be obscured within the quoted error bars.

$t/a$	$C_P(t)$	$C_S(t)$	$C_V(t)$	$C_A(t)$	$C_T(t)$	$C_X(t)$
1	$3.926(15) \times 10^{-2}$	$3.919(15) \times 10^{-2}$	$2.9286(88) \times 10^{-2}$	$2.9285(88) \times 10^{-2}$	$2.1937(41) \times 10^{-2}$	$2.1937(41) \times 10^{-2}$
2	$6.462(91) \times 10^{-3}$	$6.397(93) \times 10^{-3}$	$3.291(23) \times 10^{-3}$	$3.291(23) \times 10^{-3}$	$1.971(14) \times 10^{-3}$	$1.971(14) \times 10^{-3}$
3	$2.611(85) \times 10^{-3}$	$2.551(84) \times 10^{-3}$	$8.317(75) \times 10^{-4}$	$8.314(75) \times 10^{-4}$	$4.387(50) \times 10^{-4}$	$4.387(50) \times 10^{-4}$
4	$1.620(84) \times 10^{-3}$	$1.563(83) \times 10^{-3}$	$3.299(35) \times 10^{-4}$	$3.297(35) \times 10^{-4}$	$1.682(26) \times 10^{-4}$	$1.682(26) \times 10^{-4}$
5	$1.238(83) \times 10^{-3}$	$1.184(82) \times 10^{-3}$	$1.754(23) \times 10^{-4}$	$1.752(23) \times 10^{-4}$	$9.16(19) \times 10^{-5}$	$9.16(19) \times 10^{-5}$
6	$1.062(82) \times 10^{-3}$	$1.012(81) \times 10^{-3}$	$1.160(17) \times 10^{-4}$	$1.159(17) \times 10^{-4}$	$6.35(16) \times 10^{-5}$	$6.35(16) \times 10^{-5}$
7	$9.82(81) \times 10^{-4}$	$9.34(81) \times 10^{-4}$	$9.19(16) \times 10^{-5}$	$9.18(16) \times 10^{-5}$	$5.24(14) \times 10^{-5}$	$5.25(15) \times 10^{-5}$
8	$9.61(80) \times 10^{-4}$	$9.13(81) \times 10^{-4}$	$8.52(16) \times 10^{-5}$	$8.51(16) \times 10^{-5}$	$4.92(14) \times 10^{-5}$	$4.93(14) \times 10^{-5}$
9	$9.90(79) \times 10^{-4}$	$9.41(80) \times 10^{-4}$	$9.24(17) \times 10^{-5}$	$9.23(17) \times 10^{-5}$	$5.23(17) \times 10^{-5}$	$5.24(18) \times 10^{-5}$
10	$1.077(77) \times 10^{-3}$	$1.026(79) \times 10^{-3}$	$1.176(18) \times 10^{-4}$	$1.175(18) \times 10^{-4}$	$6.35(19) \times 10^{-5}$	$6.35(19) \times 10^{-5}$
11	$1.259(75) \times 10^{-3}$	$1.204(78) \times 10^{-3}$	$1.775(21) \times 10^{-4}$	$1.774(21) \times 10^{-4}$	$9.14(19) \times 10^{-5}$	$9.13(19) \times 10^{-5}$
12	$1.645(72) \times 10^{-3}$	$1.585(75) \times 10^{-3}$	$3.326(32) \times 10^{-4}$	$3.324(32) \times 10^{-4}$	$1.681(25) \times 10^{-4}$	$1.681(25) \times 10^{-4}$
13	$2.645(71) \times 10^{-3}$	$2.579(75) \times 10^{-3}$	$8.384(53) \times 10^{-4}$	$8.381(53) \times 10^{-4}$	$4.425(42) \times 10^{-4}$	$4.424(42) \times 10^{-4}$
14	$6.521(74) \times 10^{-3}$	$6.450(80) \times 10^{-3}$	$3.322(17) \times 10^{-3}$	$3.322(17) \times 10^{-3}$	$1.996(10) \times 10^{-3}$	$1.996(11) \times 10^{-3}$
15	$3.940(12) \times 10^{-2}$	$3.933(11) \times 10^{-2}$	$2.9396(71) \times 10^{-2}$	$2.9395(71) \times 10^{-2}$	$2.2020(44) \times 10^{-2}$	$2.2019(44) \times 10^{-2}$

**Table 6:** Time-correlation function  $C_\Gamma(t)$  of  $\bar{u}\Gamma d$  for  $P, S, V, A, T, X$  channels on the  $32^3 \times 16$  lattice with lattice spacing  $a=0.075$  fm.

$t/a$	$C_P(t)$	$C_S(t)$	$C_V(t)$	$C_A(t)$	$C_T(t)$	$C_X(t)$
1	$3.944(11) \times 10^{-2}$	$3.943(11) \times 10^{-2}$	$2.9601(71) \times 10^{-2}$	$2.9601(71) \times 10^{-2}$	$2.2085(44) \times 10^{-2}$	$2.2085(44) \times 10^{-2}$
2	$6.304(64) \times 10^{-3}$	$6.295(63) \times 10^{-3}$	$3.377(15) \times 10^{-3}$	$3.376(15) \times 10^{-3}$	$2.0059(93) \times 10^{-3}$	$2.0057(93) \times 10^{-3}$
3	$2.368(59) \times 10^{-3}$	$2.360(58) \times 10^{-3}$	$8.639(57) \times 10^{-4}$	$8.638(57) \times 10^{-4}$	$4.479(37) \times 10^{-4}$	$4.478(37) \times 10^{-4}$
4	$1.349(55) \times 10^{-3}$	$1.342(54) \times 10^{-3}$	$3.463(26) \times 10^{-4}$	$3.462(26) \times 10^{-4}$	$1.719(19) \times 10^{-4}$	$1.718(19) \times 10^{-4}$
5	$9.60(52) \times 10^{-4}$	$9.54(51) \times 10^{-4}$	$1.850(16) \times 10^{-4}$	$1.849(16) \times 10^{-4}$	$9.28(14) \times 10^{-5}$	$9.27(14) \times 10^{-5}$
6	$7.83(50) \times 10^{-4}$	$7.77(49) \times 10^{-4}$	$1.222(13) \times 10^{-4}$	$1.221(13) \times 10^{-4}$	$6.34(12) \times 10^{-5}$	$6.33(12) \times 10^{-5}$
7	$7.01(50) \times 10^{-4}$	$6.95(49) \times 10^{-4}$	$9.63(12) \times 10^{-5}$	$9.62(12) \times 10^{-5}$	$5.14(16) \times 10^{-5}$	$5.14(16) \times 10^{-5}$
8	$6.77(50) \times 10^{-4}$	$6.70(49) \times 10^{-4}$	$8.93(15) \times 10^{-5}$	$8.92(15) \times 10^{-5}$	$4.81(16) \times 10^{-5}$	$4.80(16) \times 10^{-5}$
9	$7.02(51) \times 10^{-4}$	$6.95(50) \times 10^{-4}$	$9.71(19) \times 10^{-5}$	$9.70(19) \times 10^{-5}$	$5.16(17) \times 10^{-5}$	$5.15(17) \times 10^{-5}$
10	$7.87(52) \times 10^{-4}$	$7.79(51) \times 10^{-4}$	$1.239(23) \times 10^{-4}$	$1.239(23) \times 10^{-4}$	$6.40(17) \times 10^{-5}$	$6.39(17) \times 10^{-5}$
11	$9.71(54) \times 10^{-4}$	$9.61(53) \times 10^{-4}$	$1.877(31) \times 10^{-4}$	$1.876(31) \times 10^{-4}$	$9.43(14) \times 10^{-5}$	$9.42(14) \times 10^{-5}$
12	$1.363(58) \times 10^{-3}$	$1.352(57) \times 10^{-3}$	$3.489(41) \times 10^{-4}$	$3.488(41) \times 10^{-4}$	$1.738(22) \times 10^{-4}$	$1.738(22) \times 10^{-4}$
13	$2.377(65) \times 10^{-3}$	$2.365(63) \times 10^{-3}$	$8.631(68) \times 10^{-4}$	$8.630(68) \times 10^{-4}$	$4.495(40) \times 10^{-4}$	$4.494(40) \times 10^{-4}$
14	$6.28(11) \times 10^{-3}$	$6.26(10) \times 10^{-3}$	$3.356(19) \times 10^{-3}$	$3.356(19) \times 10^{-3}$	$1.998(11) \times 10^{-3}$	$1.998(11) \times 10^{-3}$
15	$3.927(11) \times 10^{-2}$	$3.926(11) \times 10^{-2}$	$2.9478(74) \times 10^{-2}$	$2.9478(74) \times 10^{-2}$	$2.2017(45) \times 10^{-2}$	$2.2017(45) \times 10^{-2}$

**Table 7:** Time-correlation function  $C_\Gamma(t)$  of  $\bar{u}\Gamma d$  for  $P, S, V, A, T, X$  channels on the  $32^3 \times 16$  lattice with lattice spacing  $a=0.069$  fm.

$t/a$	$C_P(t)$	$C_S(t)$	$C_V(t)$	$C_A(t)$	$C_T(t)$	$C_X(t)$
1	$3.9219(97) \times 10^{-2}$	$3.9215(97) \times 10^{-2}$	$2.9480(64) \times 10^{-2}$	$2.9480(64) \times 10^{-2}$	$2.1966(39) \times 10^{-2}$	$2.1966(39) \times 10^{-2}$
2	$6.238(31) \times 10^{-3}$	$6.234(31) \times 10^{-3}$	$3.389(15) \times 10^{-3}$	$3.389(15) \times 10^{-3}$	$2.0051(86) \times 10^{-3}$	$2.0051(86) \times 10^{-3}$
3	$2.307(32) \times 10^{-3}$	$2.304(32) \times 10^{-3}$	$8.733(45) \times 10^{-4}$	$8.732(45) \times 10^{-4}$	$4.506(28) \times 10^{-4}$	$4.506(28) \times 10^{-4}$
4	$1.287(27) \times 10^{-3}$	$1.284(27) \times 10^{-3}$	$3.508(21) \times 10^{-4}$	$3.508(21) \times 10^{-4}$	$1.735(16) \times 10^{-4}$	$1.735(16) \times 10^{-4}$
5	$8.96(26) \times 10^{-4}$	$8.93(25) \times 10^{-4}$	$1.861(13) \times 10^{-4}$	$1.861(13) \times 10^{-4}$	$9.34(17) \times 10^{-5}$	$9.34(17) \times 10^{-5}$
6	$7.17(25) \times 10^{-4}$	$7.14(25) \times 10^{-4}$	$1.210(11) \times 10^{-4}$	$1.210(11) \times 10^{-4}$	$6.34(17) \times 10^{-5}$	$6.34(17) \times 10^{-5}$
7	$6.37(25) \times 10^{-4}$	$6.34(25) \times 10^{-4}$	$9.36(12) \times 10^{-5}$	$9.36(12) \times 10^{-5}$	$5.11(16) \times 10^{-5}$	$5.10(16) \times 10^{-5}$
8	$6.16(26) \times 10^{-4}$	$6.13(26) \times 10^{-4}$	$8.56(12) \times 10^{-5}$	$8.55(12) \times 10^{-5}$	$4.74(21) \times 10^{-5}$	$4.74(21) \times 10^{-5}$
9	$6.45(27) \times 10^{-4}$	$6.42(27) \times 10^{-4}$	$9.24(16) \times 10^{-5}$	$9.24(16) \times 10^{-5}$	$5.04(21) \times 10^{-5}$	$5.04(21) \times 10^{-5}$
10	$7.32(28) \times 10^{-4}$	$7.29(28) \times 10^{-4}$	$1.186(16) \times 10^{-4}$	$1.186(17) \times 10^{-4}$	$6.22(22) \times 10^{-5}$	$6.22(22) \times 10^{-5}$
11	$9.15(29) \times 10^{-4}$	$9.12(28) \times 10^{-4}$	$1.825(19) \times 10^{-4}$	$1.825(19) \times 10^{-4}$	$9.19(25) \times 10^{-5}$	$9.19(25) \times 10^{-5}$
12	$1.307(29) \times 10^{-3}$	$1.304(29) \times 10^{-3}$	$3.465(22) \times 10^{-4}$	$3.465(22) \times 10^{-4}$	$1.720(24) \times 10^{-4}$	$1.720(24) \times 10^{-4}$
13	$2.323(30) \times 10^{-3}$	$2.319(29) \times 10^{-3}$	$8.692(46) \times 10^{-4}$	$8.692(46) \times 10^{-4}$	$4.508(35) \times 10^{-4}$	$4.507(35) \times 10^{-4}$
14	$6.256(29) \times 10^{-3}$	$6.253(29) \times 10^{-3}$	$3.396(13) \times 10^{-3}$	$3.395(13) \times 10^{-3}$	$2.0141(80) \times 10^{-3}$	$2.0141(80) \times 10^{-3}$
15	$3.9292(82) \times 10^{-2}$	$3.9288(82) \times 10^{-2}$	$2.9539(54) \times 10^{-2}$	$2.9538(54) \times 10^{-2}$	$2.2012(33) \times 10^{-2}$	$2.2012(33) \times 10^{-2}$

**Table 8:** Time-correlation function  $C_\Gamma(t)$  of  $\bar{u}\Gamma d$  for  $P, S, V, A, T, X$  channels on the  $32^3 \times 16$  lattice with lattice spacing  $a=0.064$  fm.

$a$ [fm]	$T_r$ [MeV]	$\chi_S = \chi_P$	$\chi_V = \chi_A$	$\chi_T = \chi_X$
0.075	657	$4.30237\text{e-}2 \pm 1.097\text{e-}4$	$3.55848\text{e-}2 \pm 9.83\text{e-}5$	$2.94832\text{e-}2 \pm 9.25\text{e-}5$
0.069	715	$4.31394\text{e-}2 \pm 6.98\text{e-}5$	$3.57104\text{e-}2 \pm 7.26\text{e-}5$	$2.96146\text{e-}2 \pm 6.96\text{e-}5$
0.064	770	$4.32572\text{e-}2 \pm 6.79\text{e-}5$	$3.58288\text{e-}2 \pm 5.99\text{e-}5$	$2.97312\text{e-}2 \pm 5.67\text{e-}5$

**Table 9:** The bare susceptibilities (3.3) at the reference temperature  $aT_r = 1/4$ , where the chiral symmetries are completely restored with  $\chi_S = \chi_P$ ,  $\chi_V = \chi_A$  and  $\chi_T = \chi_X$  within uncertainties.

$T$ [MeV]	$a$ [fm]	$\chi_S$	$\chi_P$	$\kappa_{PS}$
164	0.075	$1.05111\text{e-}2 \pm 4.987\text{e-}4$	$1.07156\text{e-}2 \pm 5.074\text{e-}4$	$9.6326\text{e-}3 \pm 1.1575\text{e-}3$
179	0.069	$8.87705\text{e-}3 \pm 2.9615\text{e-}4$	$8.93768\text{e-}3 \pm 3.0014\text{e-}4$	$3.4031\text{e-}3 \pm 6.516\text{e-}4$
192	0.064	$8.38074\text{e-}3 \pm 1.9033\text{e-}4$	$8.41301\text{e-}3 \pm 1.9182\text{e-}4$	$1.9215\text{e-}3 \pm 4.227\text{e-}4$
219	0.075	$7.18393\text{e-}3 \pm 2.2556\text{e-}4$	$7.22016\text{e-}3 \pm 2.2685\text{e-}4$	$2.5150\text{e-}3 \pm 3.733\text{e-}4$
238	0.069	$6.79871\text{e-}3 \pm 1.3377\text{e-}4$	$6.80861\text{e-}3 \pm 1.3413\text{e-}4$	$7.2799\text{e-}4 \pm 1.6966\text{e-}4$
257	0.064	$6.37147\text{e-}3 \pm 1.4598\text{e-}4$	$6.37588\text{e-}3 \pm 1.4585\text{e-}4$	$3.4584\text{e-}4 \pm 1.5903\text{e-}4$
263	0.075	$5.09703\text{e-}3 \pm 1.1363\text{e-}4$	$5.10731\text{e-}3 \pm 1.1327\text{e-}4$	$1.0073\text{e-}3 \pm 2.848\text{e-}4$
286	0.069	$5.13759\text{e-}3 \pm 1.0258\text{e-}4$	$5.14099\text{e-}3 \pm 1.0258\text{e-}4$	$3.3068\text{e-}4 \pm 1.0571\text{e-}4$
308	0.064	$5.12178\text{e-}3 \pm 1.4051\text{e-}4$	$5.12323\text{e-}3 \pm 1.4056\text{e-}4$	$1.4156\text{e-}4 \pm 7.319\text{e-}5$
328	0.075	$4.06493\text{e-}3 \pm 1.2288\text{e-}4$	$4.06844\text{e-}3 \pm 1.2274\text{e-}4$	$4.3120\text{e-}4 \pm 1.0000\text{e-}4$
357	0.069	$3.90275\text{e-}3 \pm 1.5754\text{e-}4$	$3.90364\text{e-}3 \pm 1.5779\text{e-}4$	$1.1457\text{e-}4 \pm 4.094\text{e-}5$
385	0.064	$4.04070\text{e-}3 \pm 1.1231\text{e-}4$	$4.04106\text{e-}3 \pm 1.1233\text{e-}4$	$4.4588\text{e-}5 \pm 1.3679\text{e-}5$

**Table 10:** Scalar and pseudoscalar (regularized) susceptibilities  $\chi_S$ ,  $\chi_P$  and the RG-invariant symmetry ratio  $\kappa_{PS}$  for three lattice spacings and twelve temperatures.

$T$ [MeV]	$a$ [fm]	$\chi_V$	$\chi_A$	$\kappa_{VA}$
164	0.075	$1.34902\text{e-}3 \pm 8.544\text{e-}5$	$1.35069\text{e-}3 \pm 8.541\text{e-}5$	$6.2136\text{e-}4 \pm 7.344\text{e-}5$
179	0.069	$1.12135\text{e-}3 \pm 7.922\text{e-}5$	$1.12228\text{e-}3 \pm 7.921\text{e-}5$	$4.1380\text{e-}4 \pm 4.778\text{e-}5$
192	0.064	$1.26691\text{e-}3 \pm 6.697\text{e-}5$	$1.26739\text{e-}3 \pm 6.696\text{e-}5$	$1.8739\text{e-}4 \pm 2.175\text{e-}5$
219	0.075	$1.41705\text{e-}3 \pm 8.073\text{e-}5$	$1.41765\text{e-}3 \pm 8.070\text{e-}5$	$2.1163\text{e-}4 \pm 4.388\text{e-}5$
238	0.069	$1.22632\text{e-}3 \pm 6.456\text{e-}5$	$1.22665\text{e-}3 \pm 6.456\text{e-}5$	$1.3218\text{e-}4 \pm 1.796\text{e-}5$
257	0.064	$1.22084\text{e-}3 \pm 6.698\text{e-}5$	$1.22096\text{e-}3 \pm 6.698\text{e-}5$	$5.0740\text{e-}5 \pm 6.763\text{e-}6$
263	0.075	$1.37866\text{e-}3 \pm 6.513\text{e-}5$	$1.37894\text{e-}3 \pm 6.513\text{e-}5$	$1.0359\text{e-}4 \pm 9.46\text{e-}6$
286	0.069	$1.23223\text{e-}3 \pm 5.534\text{e-}5$	$1.23238\text{e-}3 \pm 5.533\text{e-}5$	$6.3550\text{e-}5 \pm 8.184\text{e-}6$
308	0.064	$1.10158\text{e-}3 \pm 8.783\text{e-}5$	$1.10163\text{e-}3 \pm 8.783\text{e-}5$	$2.2720\text{e-}5 \pm 5.880\text{e-}6$
328	0.075	$1.38667\text{e-}3 \pm 6.475\text{e-}5$	$1.38681\text{e-}3 \pm 6.475\text{e-}5$	$5.0800\text{e-}5 \pm 6.462\text{e-}6$
357	0.069	$1.22921\text{e-}3 \pm 8.492\text{e-}5$	$1.22927\text{e-}3 \pm 8.492\text{e-}5$	$2.5474\text{e-}5 \pm 6.958\text{e-}6$
385	0.064	$1.04074\text{e-}3 \pm 7.222\text{e-}5$	$1.04076\text{e-}3 \pm 7.222\text{e-}5$	$1.0811\text{e-}5 \pm 3.300\text{e-}6$

**Table 11:** Vector and axial-vector (regularized) susceptibilities  $\chi_V$ ,  $\chi_A$  and the RG-invariant symmetry ratio  $\kappa_{VA}$  for three lattice spacings and twelve temperatures.

$T[\text{MeV}]$	$a[\text{fm}]$	$\chi_T$	$\chi_X$	$\kappa_{TX}$
164	0.075	$4.67899\text{e-}3 \pm 5.103\text{e-}5$	$4.68006\text{e-}3 \pm 5.109\text{e-}5$	$1.1465\text{e-}4 \pm 2.728\text{e-}5$
179	0.069	$4.72086\text{e-}3 \pm 4.586\text{e-}5$	$4.72150\text{e-}3 \pm 4.587\text{e-}5$	$6.7956\text{e-}5 \pm 2.4404\text{e-}5$
192	0.064	$4.89019\text{e-}3 \pm 3.728\text{e-}5$	$4.89052\text{e-}3 \pm 3.728\text{e-}5$	$3.3596\text{e-}5 \pm 5.709\text{e-}6$
219	0.075	$4.55929\text{e-}3 \pm 4.561\text{e-}5$	$4.55968\text{e-}3 \pm 4.561\text{e-}5$	$4.3281\text{e-}5 \pm 5.064\text{e-}6$
238	0.069	$4.65637\text{e-}3 \pm 4.697\text{e-}5$	$4.65660\text{e-}3 \pm 4.697\text{e-}5$	$2.4904\text{e-}5 \pm 3.759\text{e-}6$
257	0.064	$4.64978\text{e-}3 \pm 3.895\text{e-}5$	$4.64988\text{e-}3 \pm 3.894\text{e-}5$	$1.0413\text{e-}5 \pm 2.459\text{e-}6$
263	0.075	$4.33531\text{e-}3 \pm 3.974\text{e-}5$	$4.33550\text{e-}3 \pm 3.975\text{e-}5$	$2.1880\text{e-}5 \pm 3.017\text{e-}6$
286	0.069	$4.37743\text{e-}3 \pm 3.145\text{e-}5$	$4.37756\text{e-}3 \pm 3.145\text{e-}5$	$1.4875\text{e-}5 \pm 2.079\text{e-}6$
308	0.064	$4.34406\text{e-}3 \pm 5.208\text{e-}5$	$4.34411\text{e-}3 \pm 5.208\text{e-}5$	$6.2172\text{e-}6 \pm 6.220\text{e-}7$
328	0.075	$4.12041\text{e-}3 \pm 4.336\text{e-}5$	$4.12052\text{e-}3 \pm 4.336\text{e-}5$	$1.4027\text{e-}5 \pm 3.257\text{e-}6$
357	0.069	$3.99545\text{e-}3 \pm 5.058\text{e-}5$	$3.99551\text{e-}3 \pm 5.058\text{e-}5$	$8.0070\text{e-}6 \pm 7.180\text{e-}7$
385	0.064	$3.94033\text{e-}3 \pm 4.523\text{e-}5$	$3.94037\text{e-}3 \pm 4.523\text{e-}5$	$4.0301\text{e-}6 \pm 6.117\text{e-}7$

**Table 12:** Tensor-vector and axial-tensor-vector (regularized) susceptibilities  $\chi_T$ ,  $\chi_X$  and the RG-invariant symmetry ratio  $\kappa_{TX}$  for three lattice spacings and twelve temperatures.

## Acknowledgments

We are grateful to Academia Sinica Grid Computing Center and National Center for High Performance Computing for the computer time and facilities. This work was supported by the National Science and Technology Council (Grants No. 108-2112-M-003-005, No. 109-2112-M-003-006, No. 110-2112-M-003-009), and Academia Sinica Grid Computing Centre (Grant No. AS-CFII-112-103).

## References

- [1] Y. Nambu and G. Jona-Lasinio, “Dynamical model of elementary particles based on an analogy with Superconductivity. 1.”, *Phys. Rev.* **122**, 345-358 (1961)
- [2] Y. Nambu and G. Jona-Lasinio, “Dynamical model of elementary particles based on an analogy with superconductivity. II.”, *Phys. Rev.* **124**, 246-254 (1961)
- [3] S. L. Adler, “Axial vector vertex in spinor electrodynamics”, *Phys. Rev.* **177**, 2426-2438 (1969)
- [4] J. S. Bell and R. Jackiw, “A PCAC puzzle:  $\pi^0 \rightarrow \gamma\gamma$  in the  $\sigma$  model”, *Nuovo Cim. A* **60**, 47-61 (1969)
- [5] K. Fujikawa, “Path Integral Measure for Gauge Invariant Fermion Theories”, *Phys. Rev. Lett.* **42**, 1195-1198 (1979)
- [6] G. 't Hooft, “Computation of the Quantum Effects Due to a Four-Dimensional Pseudoparticle”, *Phys. Rev. D* **14**, 3432-3450 (1976) [erratum: *Phys. Rev. D* **18**, 2199 (1978)]
- [7] E. Witten, “Current Algebra Theorems for the U(1) Goldstone Boson”, *Nucl. Phys. B* **156**, 269-283 (1979)
- [8] G. Veneziano, “U(1) Without Instantons”, *Nucl. Phys. B* **159**, 213-224 (1979)
- [9] Y. Aoki, G. Endrodi, Z. Fodor, S. D. Katz and K. K. Szabo, “The Order of the quantum chromodynamics transition predicted by the standard model of particle physics”, *Nature* **443**, 675-678 (2006) [arXiv:hep-lat/0611014 [hep-lat]].
- [10] S. Borsanyi, Z. Fodor, C. Hoelbling, S. D. Katz, S. Krieg and K. K. Szabo, “Full result for the QCD equation of state with 2+1 flavors”, *Phys. Lett. B* **730**, 99-104 (2014) [arXiv:1309.5258 [hep-lat]].
- [11] A. Bazavov *et al.* [HotQCD], “Equation of state in ( 2+1 )-flavor QCD”, *Phys. Rev. D* **90**, 094503 (2014) [arXiv:1407.6387 [hep-lat]].
- [12] A. Bazavov *et al.* [HotQCD], “Chiral crossover in QCD at zero and non-zero chemical potentials”, *Phys. Lett. B* **795**, 15-21 (2019) [arXiv:1812.08235 [hep-lat]].
- [13] S. Borsanyi, Z. Fodor, J. N. Guenther, R. Kara, S. D. Katz, P. Parotto, A. Pasztor, C. Ratti and K. K. Szabo, “QCD Crossover at Finite Chemical Potential from Lattice Simulations”, *Phys. Rev. Lett.* **125**, no.5, 052001 (2020) [arXiv:2002.02821 [hep-lat]].
- [14] R. D. Pisarski and F. Wilczek, “Remarks on the Chiral Phase Transition in Chromodynamics”, *Phys. Rev. D* **29**, 338-341 (1984)
- [15] H. Leutwyler and A. V. Smilga, “Spectrum of Dirac operator and role of winding number in QCD”, *Phys. Rev. D* **46**, 5607-5632 (1992)

- [16] T. D. Cohen, “QCD inequalities, the high temperature phase of QCD, and  $U(1)_A$  symmetry”, *Phys. Rev. D* **54**, R1867-R1870 (1996) [arXiv:hep-ph/9601216 [hep-ph]].
- [17] S. Aoki, H. Fukaya and Y. Taniguchi, “Chiral symmetry restoration, eigenvalue density of Dirac operator and axial  $U(1)$  anomaly at finite temperature”, *Phys. Rev. D* **86**, 114512 (2012) [arXiv:1209.2061 [hep-lat]].
- [18] G. Cossu, S. Aoki, H. Fukaya, S. Hashimoto, T. Kaneko, H. Matsufuru and J. I. Noaki, “Finite temperature study of the axial  $U(1)$  symmetry on the lattice with overlap fermion formulation,” *Phys. Rev. D* **87**, no.11, 114514 (2013) [erratum: *Phys. Rev. D* **88**, no.1, 019901 (2013)] [arXiv:1304.6145 [hep-lat]].
- [19] M. I. Buchoff, M. Cheng, N. H. Christ, H. T. Ding, C. Jung, F. Karsch, Z. Lin, R. D. Mawhinney, S. Mukherjee and P. Petreczky, *et al.* “QCD chiral transition,  $U(1)_A$  symmetry and the dirac spectrum using domain wall fermions”, *Phys. Rev. D* **89**, no.5, 054514 (2014) [arXiv:1309.4149 [hep-lat]].
- [20] B. B. Brandt, A. Francis, H. B. Meyer, O. Philipsen, D. Robaina and H. Wittig, “On the strength of the  $U_A(1)$  anomaly at the chiral phase transition in  $N_f = 2$  QCD”, *JHEP* **12**, 158 (2016) [arXiv:1608.06882 [hep-lat]].
- [21] A. Tomiya, G. Cossu, S. Aoki, H. Fukaya, S. Hashimoto, T. Kaneko and J. Noaki, “Evidence of effective axial  $U(1)$  symmetry restoration at high temperature QCD”, *Phys. Rev. D* **96**, no.3, 034509 (2017); **96**, A079902 (2017). [arXiv:1612.01908 [hep-lat]].
- [22] H. T. Ding, S. T. Li, S. Mukherjee, A. Tomiya, X. D. Wang and Y. Zhang, “Correlated Dirac Eigenvalues and Axial Anomaly in Chiral Symmetric QCD”, *Phys. Rev. Lett.* **126**, no.8, 082001 (2021) [arXiv:2010.14836 [hep-lat]].
- [23] O. Kaczmarek, R. Shanker and S. Sharma, “Eigenvalues of the QCD Dirac matrix with improved staggered quarks in the continuum limit”, *Phys. Rev. D* **108**, no.9, 094501 (2023) [arXiv:2301.11610 [hep-lat]].
- [24] S. Aoki *et al.* [JLQCD], “Study of the axial  $U(1)$  anomaly at high temperature with lattice chiral fermions”, *Phys. Rev. D* **103**, no.7, 074506 (2021) [arXiv:2011.01499 [hep-lat]].
- [25] T. W. Chiu, “Symmetries of meson correlators in high-temperature QCD with physical (u/d,s,c) domain-wall quarks”, *Phys. Rev. D* **107**, no.11, 114501 (2023) [arXiv:2302.06073 [hep-lat]].
- [26] R. V. Gavai, M. E. Jaensch, O. Kaczmarek, F. Karsch, M. Sarkar, R. Shanker, S. Sharma, S. Sharma and T. Ueding, “Aspects of the chiral crossover transition in (2+1)-flavor QCD with Möbius domain-wall fermions”, *Phys. Rev. D* **111**, no.3, 034507 (2025) [arXiv:2411.10217 [hep-lat]].
- [27] H. T. Ding, “Lattice QCD at finite temperature and density,” [arXiv:2603.16230 [hep-lat]].
- [28] D. B. Kaplan, “A Method for simulating chiral fermions on the lattice”, *Phys. Lett. B* **288**, 342-347 (1992) [arXiv:hep-lat/9206013 [hep-lat]].
- [29] D. B. Kaplan, “Chiral fermions on the lattice”, *Nucl. Phys. B Proc. Suppl.* **30**, 597-600 (1993)
- [30] H. Neuberger, “Exactly massless quarks on the lattice”, *Phys. Lett. B* **417**, 141-144 (1998) [arXiv:hep-lat/9707022 [hep-lat]].
- [31] R. Narayanan and H. Neuberger, “A Construction of lattice chiral gauge theories”, *Nucl. Phys. B* **443**, 305-385 (1995) [arXiv:hep-th/9411108 [hep-th]].

- [32] T. W. Chiu, “Symmetries of spatial correlators of light and heavy mesons in high temperature lattice QCD”, *Phys. Rev. D* **110**, no.1, 014502 (2024) [arXiv:2404.15932 [hep-lat]].
- [33] T. W. Chiu, “Symmetries in High-Temperature Lattice QCD with (u, d, s, c, b) Optimal Domain-Wall Quarks”, *Symmetry* **17**, no.5, 700 (2025) [arXiv:2411.16705 [hep-lat]].
- [34] G. Martinelli, C. Pittori, C. T. Sachrajda, M. Testa and A. Vladikas, “A general method for nonperturbative renormalization of lattice operators”, *Nucl. Phys. B* **445**, 81-108 (1995) [arXiv:hep-lat/9411010 [hep-lat]].
- [35] S. A. Larin, “The Renormalization of the axial anomaly in dimensional regularization,” *Phys. Lett. B* **303**, 113-118 (1993) [arXiv:hep-ph/9302240 [hep-ph]].
- [36] L. Dolan and R. Jackiw, “Symmetry Behavior at Finite Temperature,” *Phys. Rev. D* **9**, 3320-3341 (1974)
- [37] S. Weinberg, “Gauge and Global Symmetries at High Temperature,” *Phys. Rev. D* **9**, 3357-3378 (1974)
- [38] C. W. Bernard, “Feynman Rules for Gauge Theories at Finite Temperature,” *Phys. Rev. D* **9**, 3312-3319 (1974)
- [39] M. B. Kislinger and P. D. Morley, “Collective Phenomena in Gauge Theories. 2. Renormalization in Finite Temperature Field Theory,” *Phys. Rev. D* **13**, 2771 (1976)
- [40] N. P. Landsman and C. G. van Weert, “Real and Imaginary Time Field Theory at Finite Temperature and Density,” *Phys. Rept.* **145**, 141 (1987)
- [41] T. W. Chiu, “Optimal lattice domain wall fermions”, *Phys. Rev. Lett.* **90**, 071601 (2003) [hep-lat/0209153];
- [42] T. W. Chiu, “Domain-Wall Fermion with  $R_5$  Symmetry”, *Phys. Lett. B* **744**, 95 (2015) [arXiv:1503.01750 [hep-lat]].
- [43] K. G. Wilson, “Confinement of Quarks”, *Phys. Rev. D* **10**, 2445-2459 (1974)
- [44] T. W. Chiu, T. H. Hsieh, Y. Y. Mao [TWQCD Collaboration], “Pseudoscalar Meson in Two Flavors QCD with the Optimal Domain-Wall Fermion”, *Phys. Lett. B* **717**, 420 (2012) [arXiv:1109.3675 [hep-lat]].
- [45] Y. C. Chen, T. W. Chiu [TWQCD Collaboration], “Exact Pseudofermion Action for Monte Carlo Simulation of Domain-Wall Fermion”, *Phys. Lett. B* **738**, 55 (2014) [arXiv:1403.1683 [hep-lat]].
- [46] Y. C. Chen, T. W. Chiu and T. H. Hsieh [TWQCD Collaboration], “Topological susceptibility in finite temperature QCD with physical (u/d,s,c) domain-wall quarks”, *Phys. Rev. D* **106**, no.7, 074501 (2022) [arXiv:2204.01556 [hep-lat]].
- [47] R. Narayanan and H. Neuberger, “Infinite N phase transitions in continuum Wilson loop operators”, *JHEP* **0603**, 064 (2006) [hep-th/0601210].
- [48] M. Luscher, “Properties and uses of the Wilson flow in lattice QCD”, *JHEP* **1008**, 071 (2010); Erratum: [*JHEP* **1403**, 092 (2014)] [arXiv:1006.4518 [hep-lat]].
- [49] A. Bazavov *et al.* [MILC Collaboration], “Gradient flow and scale setting on MILC HISQ ensembles”, *Phys. Rev. D* **93**, no. 9, 094510 (2016) [arXiv:1503.02769 [hep-lat]].
- [50] Y. C. Chen, T. W. Chiu [TWQCD Collaboration], “Chiral Symmetry and the Residual Mass in Lattice QCD with the Optimal Domain-Wall Fermion”, *Phys. Rev. D* **86**, 094508 (2012) [arXiv:1205.6151 [hep-lat]].

- [51] T. W. Chiu, “Ginsparg-Wilson fermion propagators and chiral condensate”, *Phys. Rev. D* **60**, 034503 (1999) [arXiv:hep-lat/9810052 [hep-lat]].
- [52] P. Petreczky, H. P. Schadler and S. Sharma, “The topological susceptibility in finite temperature QCD and axion cosmology”, *Phys. Lett. B* **762**, 498-505 (2016) [arXiv:1606.03145 [hep-lat]].
- [53] S. Borsanyi, Z. Fodor, J. Guenther, K. H. Kampert, S. D. Katz, T. Kawanai, T. G. Kovacs, S. W. Mages, A. Pasztor and F. Pittler, *et al.* “Calculation of the axion mass based on high-temperature lattice quantum chromodynamics”, *Nature* **539**, no.7627, 69-71 (2016) [arXiv:1606.07494 [hep-lat]].
- [54] A. Athenodorou, C. Bonanno, C. Bonati, G. Clemente, F. D’Angelo, M. D’Elia, L. Maio, G. Martinelli, F. Sanfilippo and A. Todaro, “Topological susceptibility of  $N_f = 2 + 1$  QCD from staggered fermions spectral projectors at high temperatures”, *JHEP* **10**, 197 (2022) [arXiv:2208.08921 [hep-lat]].
- [55] A. Y. Kotov, M. P. Lombardo and A. Trunin, “Topological observables and  $\theta$  dependence in high temperature QCD from lattice simulations”, *JHEP* **09**, 045 (2025) [arXiv:2502.15407 [hep-lat]].
- [56] Y. Y. Mao and T. W. Chiu [TWQCD Collaboration], “Topological Susceptibility to the One-Loop Order in Chiral Perturbation Theory,” *Phys. Rev. D* **80**, 034502 (2009) [arXiv:0903.2146 [hep-lat]].
- [57] D. J. Gross, R. D. Pisarski and L. G. Yaffe, “QCD and Instantons at Finite Temperature”, *Rev. Mod. Phys.* **53**, 43 (1981)
- [58] L. Y. Glozman, “SU(4) symmetry of the dynamical QCD string and genesis of hadron spectra, *Eur. Phys. J. A* **51**, no.3, 27 (2015) [arXiv:1407.2798 [hep-ph]].
- [59] C. Rohrhofer, Y. Aoki, G. Cossu, H. Fukaya, C. Gattringer, L. Y. Glozman, S. Hashimoto, C. B. Lang and S. Prelovsek, “Symmetries of spatial meson correlators in high temperature QCD”, *Phys. Rev. D* **100**, no.1, 014502 (2019) [arXiv:1902.03191 [hep-lat]].
- [60] C. Rohrhofer, Y. Aoki, L. Y. Glozman and S. Hashimoto, “Chiral-spin symmetry of the meson spectral function above  $T_c$ ”, *Phys. Lett. B* **802**, 135245 (2020) [arXiv:1909.00927 [hep-lat]].
- [61] A. Alexandru and I. Horváth, “Possible New Phase of Thermal QCD,” *Phys. Rev. D* **100**, no.9, 094507 (2019) [arXiv:1906.08047 [hep-lat]].
- [62] X. L. Meng *et al.* [ $\chi$ QCD and CLQCD], “Separation of infrared and bulk in thermal QCD”, *JHEP* **12**, 101 (2024) [arXiv:2305.09459 [hep-lat]].
- [63] G. ’t Hooft, “On the Phase Transition Towards Permanent Quark Confinement,” *Nucl. Phys. B* **138**, 1-25 (1978)
- [64] J. A. Mickley, C. Allton, R. Bignell and D. B. Leinweber, “Center vortex evidence for a second finite-temperature QCD transition”, *Phys. Rev. D* **111**, no.3, 034508 (2025) [arXiv:2411.19446 [hep-lat]].
- [65] A. Pelissetto and E. Vicari, “Relevance of the axial anomaly at the finite-temperature chiral transition in QCD”, *Phys. Rev. D* **88**, no.10, 105018 (2013) [arXiv:1309.5446 [hep-lat]].
- [66] J. P. Klinger, R. Kaiser and O. Philipsen, “The order of the chiral phase transition in massless many-flavour lattice QCD,” *PoS LATTICE2024*, 172 (2025) [arXiv:2501.19251 [hep-lat]].

- [67] A. Y. Kotov, M. P. Lombardo and A. Trunin, “QCD transition at the physical point, and its scaling window from twisted mass Wilson fermions,” [Phys. Lett. B \*\*823\*\*, 136749 \(2021\)](#) [arXiv:2105.09842 [hep-lat]].
- [68] J. Braun, W. j. Fu, J. M. Pawłowski, F. Rennecke, D. Rosenblüh and S. Yin, “Chiral susceptibility in (2+1)-flavor QCD”, [Phys. Rev. D \*\*102\*\*, no.5, 056010 \(2020\)](#) [arXiv:2003.13112 [hep-ph]].